Mathematical Models and Methods in Applied Sciences
Vol. 35, No. 9 (2025) 2013–2045

DOI: 10.1142/S0218202525500253

World Scientific
www.worldscientific.com

High-order compact splitting spectral methods for the rotating spin-1 Bose–Einstein condensates in a magnetic field

Xin Liu* and Xiangyu Meng†

Center for Applied Mathematics and KL-AAGDM, Tianjin University, Tianjin 300072, P. R. China
**liuxin_921@tju.edu.cn*
†*xiangyumeng1004@163.com*

Qinglin Tang

School of Mathematics, Sichuan University, Chengdu 610064, P. R. China
qinglin_tang@scu.edu.cn

Yong Zhang‡

Center for Applied Mathematics and KL-AAGDM, Tianjin University, Tianjin 300072, P. R. China
Zhang_Yong@tju.edu.cn

Received 21 December 2024
Accepted 29 March 2025
Published 28 May 2025
Communicated by Nicola Bellomo, Franco Brezzi and Weizhu Bao

We propose high-order compact splitting Fourier spectral methods to compute the dynamics of rotating spin-1 Bose–Einstein condensates (BECs) under an Ioffe-Pritchard magnetic field. We split the Hamiltonian into a linear part, which consists of the Laplace, rotation and Zeeman energy terms, and a nonlinear part, which includes all the remaining terms. This "compact" splitting, involving only two operators, significantly simplifies the construction of high-order schemes. For the linear subproblem, we factorize the linear operator as a product of simple sub-operators using the exact classical-quantum correspondence and semigroups decomposition, and such sub-operators are well approximated by Fourier spectral method and integrated exactly in phase space as usual. Importantly and surprisingly, the splitting coefficients, originally determined by a nonlinear equation, can actually be computed exactly by solving a linear system, ending up with explicit formulas. For the nonlinear subproblem, we derive an exact formula of the spin vector, which is not conserved in presence of the magnetic field, and transform it into a linear problem. Then we design explicit high-order schemes using Magnus integrators. Our scheme achieves spectral accuracy in space and high-order precision in time with near-optimal efficiency. It is explicit, easy to implement and unconditionally stable. In

‡Corresponding author

addition, we derive some properties of our numerical scheme and conduct a comprehensive investigation, including accuracy confirmation, efficiency test, property verification, interaction of quantized vortices and dynamics under honeycomb potential.

Keywords: Spin-1 Bose–Einstein condensate; dynamics; rotating; compact operator splitting scheme; Fourier spectral method.

AMS Subject Classification: 35Q41, 65M70, 81Q05, 81V45

1. Introduction

Since its first observation in 1995,[2, 15] the Bose–Einstein condensation (BEC) has provided an incredible glimpse into the macroscopic quantum world. At early stage, atoms were confined in magnetic traps and the spin degrees of freedom were frozen. The particles are described by a scalar model and the wave function is governed by the Gross–Pitaevskii equation (GPE) within the mean-field approximation.[4, 16] Recently, the development of optical trapping techniques has enabled to confine atoms independently of their spin orientation and thus so-called spinor condensates. The spin-1 BEC was realized experimentally in ^{23}Na and ^{87}Rb.[17, 28] In contrast to a scalar BEC, the spin-F BEC is described by the coupled GPEs, which consists of $2F+1$ ($F \in \mathbb{N}$) equations, and each governs one of the $2F+1$ hyperfine states ($m_F = -F, -F+1, \ldots, F-1, F$) within the mean field approximation.[18, 19, 23] In fact, experimental achievements of spinor BECs have created great opportunities to study the abundant quantum phenomena that are absent in scalar BECs.[5, 30]

For temperatures below the critical temperature, the dynamics of the rotating spin-1 BEC are well described by the dimensionless coupled Gross–Pitaevskii equations (CGPEs) with an angular momentum rotational term in the d-dimension ($d = 2$ or $d = 3$)[6, 8, 11, 20]

$$i\partial_t \psi_1(\mathbf{x},t) = \left[-\frac{1}{2}\nabla^2 + V(\mathbf{x}) + E_1 - \Omega L_z + \beta_n\rho + \beta_s(\rho_1+\rho_0-\rho_{-1})\right]\psi_1 + \beta_s\bar{\psi}_{-1}\psi_0^2 + B\psi_0, \tag{1.1}$$

$$i\partial_t \psi_0(\mathbf{x},t) = \left[-\frac{1}{2}\nabla^2 + V(\mathbf{x}) + E_0 - \Omega L_z + \beta_n\rho + \beta_s(\rho_1+\rho_{-1})\right]\psi_0 + 2\beta_s\psi_1\psi_{-1}\bar{\psi}_0 + B(\psi_1+\psi_{-1}), \tag{1.2}$$

$$i\partial_t \psi_{-1}(\mathbf{x},t) = \left[-\frac{1}{2}\nabla^2 + V(\mathbf{x}) + E_{-1} - \Omega L_z + \beta_n\rho + \beta_s(\rho_0+\rho_{-1}-\rho_1)\right]\psi_{-1} + \beta_s\bar{\psi}_1\psi_0^2 + B\psi_0, \tag{1.3}$$

$$\psi_\ell(\mathbf{x},0) = \psi_\ell^0(\mathbf{x}), \quad \ell = 1, 0, -1. \tag{1.4}$$

Here, $\mathbf{x} = (x,y,z)^\top \in \mathbb{R}^3$ or $\mathbf{x} = (x,y)^\top \in \mathbb{R}^2$ and t is the time. $\Psi := (\psi_1, \psi_0, \psi_{-1})^\top$ is the three-component wave function, and $\rho = \rho_1 + \rho_0 + \rho_{-1}$ is the total density

with $\rho_\ell = |\psi_\ell|^2$ ($\ell = 1, 0, -1$) being the density of ℓth component. $L_z = i(y\partial_x - x\partial_y)$ is the z-component of the angular momentum and Ω represents the rotation speed. $E_\ell \in \mathbb{R}$ is the Zeeman energy, $B \in \mathbb{R}$ is the external Ioffe-Pritchard magnetic field, and β_n and β_s are the mean-field and spin-exchange interaction constants respectively. $\bar{f}$ denotes the conjugate of the function f. In most experiments, $V(\mathbf{x})$ is usually chosen as the harmonic potential, i.e.

$$V(\mathbf{x}) = \frac{1}{2}\begin{cases}\gamma_x^2 x^2 + \gamma_y^2 y^2, & d = 2,\\ \gamma_x^2 x^2 + \gamma_y^2 y^2 + \gamma_z^2 z^2, & d = 3,\end{cases} \tag{1.5}$$

with γ_v ($v = x, y, z$) being the trapping frequency in the v-direction.

Introduce the spin-1 matrices $\mathbf{f} := (f_x, f_y, f_z)^\top$ as

$$f_x = \frac{1}{\sqrt{2}}\begin{pmatrix}0 & 1 & 0\\ 1 & 0 & 1\\ 0 & 1 & 0\end{pmatrix}, \quad f_y = \frac{i}{\sqrt{2}}\begin{pmatrix}0 & -1 & 0\\ 1 & 0 & -1\\ 0 & 1 & 0\end{pmatrix}, \quad f_z = \begin{pmatrix}1 & 0 & 0\\ 0 & 0 & 0\\ 0 & 0 & -1\end{pmatrix}, \tag{1.6}$$

and the spin vector $\mathbf{F} := (F_x(\Psi), F_y(\Psi), F_z(\Psi))^\top := (\Psi^{\mathsf{H}} f_x \Psi, \Psi^{\mathsf{H}} f_y \Psi, \Psi^{\mathsf{H}} f_z \Psi)^\top$, where Ψ^{H} is the conjugate transpose of Ψ, then the CGPEs (1.1)–(1.3) are reformulated in the compact form shown below

$$\begin{aligned} i\partial_t \Psi &= \mathcal{H}\Psi\\ &:= \left[\left(-\frac{1}{2}\nabla^2 + V - \Omega L_z + \beta_n \rho\right) I_3 + \operatorname{diag}\{E_1, E_0, E_{-1}\} + \beta_s \mathbf{F}\cdot\mathbf{f} + \mathbf{B}\right]\Psi, \end{aligned} \tag{1.7}$$

where $\mathcal{H}$ is the Hamiltonian with I_3 being the 3×3 identity matrix and

$$\mathbf{F}\cdot\mathbf{f} = \begin{pmatrix} F_z & \frac{1}{\sqrt{2}}F_- & 0\\ \frac{1}{\sqrt{2}}F_+ & 0 & \frac{1}{\sqrt{2}}F_-\\ 0 & \frac{1}{\sqrt{2}}F_+ & -F_z\end{pmatrix}, \quad \mathbf{B} = \begin{pmatrix}0 & B & 0\\ B & 0 & B\\ 0 & B & 0\end{pmatrix},$$

with $F_\pm = F_x \pm iF_y$.

Two important invariants of the time-dependent CGPEs (1.1)–(1.3) are the *mass* (or *normalization*) of the wave function

$$N(t) := N(\Psi(\cdot, t)) := \int_{\mathbb{R}^d} \sum_{\ell=-1}^{1} |\psi_\ell(\mathbf{x}, t)|^2 \mathrm{d}\mathbf{x} \equiv N(\Psi(\cdot, 0)) = 1, \quad t \geq 0 \tag{1.8}$$

and the *energy per particle*

$$E(t) := E(\Psi(\cdot,t)) = \int_{\mathbb{R}^d} \Bigg[\sum_{\ell=-1}^{1} \left(\frac{1}{2}|\nabla\psi_\ell|^2 + (V(\mathbf{x}) + E_\ell)|\psi_\ell|^2 - \Omega\bar{\psi}_\ell L_z \psi_\ell \right) + \frac{\beta_n}{2}\rho^2 + \frac{\beta_s}{2}(|F_+|^2 + |F_z|^2) + 2B\,\mathrm{Re}(\bar{\psi}_0(\psi_1 + \psi_{-1})) \Bigg] \mathrm{d}\mathbf{x} \equiv E(\Psi(\cdot,0)), \quad t \geq 0. \tag{1.9}$$

When $B = 0$, another important invariant is the total *magnetization*

$$M(t) = M(\Psi(\cdot,t)) := \sum_{\ell=-1}^{1} \int_{\mathbb{R}^d} \ell\,|\psi_\ell(\mathbf{x},t)|^2\,\mathrm{d}\mathbf{x} \equiv M(\Psi(\cdot,0)), \quad t \geq 0. \tag{1.10}$$

There is vast literature on mathematical and numerical studies of the dynamics for scalar BEC, and we direct readers to Refs. 3, 5, 9, 10, 14 and 37 for further information. Along the numerical front, the time-splitting Fourier spectral method is one of the most popular methods due to its efficiency, stability and implementation simplicity. This method has been applied to spinor BECs.[4, 11, 34–36] For the rotating spin-1 BEC, Bao *et al.*[7, 11] and Wang[36] proposed a second-order spectrally accurate numerical method, where they all split the Hamiltonian into three parts. In Refs. 11 and 36, they grouped the Laplace and rotation term as a linear part, and the linear subproblem was solved either by finite difference/element in polar and spherical coordinates or by Alternating Direction Implicit (ADI) combined with Fourier spectral method. In Ref. 7, they grouped the Laplace, rotation and radial/cylindrical symmetric part of trapping potential as a linear part, and solve it using generalized Laguerre–Fourier–Hermite spectral method in polar/cylindrical coordinates on the whole space. To efficiently investigate the fine structures of such rotating systems, including vortex lines and/or vortex lattice, it is advantageous to employ high-order schemes. However, it is somewhat complicated to construct high-order schemes with such three subproblems. It will be much easier if the Hamiltonian is split into two operators,[38] and we shall refer such splitting with fewer operators as "compact" splitting hereafter.[34, 35]

As far as we know, there are very limited research on compact splitting for spinor BECs. For dynamics of spinor BECs without rotation term, Symes *et al.* proposed a compact splitting scheme for spin-1 and spin-2 BECs,[34, 35] where the nonlinear subproblem was integrated analytically in physical space and the linear operator was integrated in phase space. Recently, for rotating spin-1 BEC with the spin-orbit coupling (SOC), Liu *et al.* proposed a high-order compact splitting scheme, where the Hamiltonian is split into two parts, and both subproblems are integrated exactly.[26] For rotating spinor BEC, there is no simple way to split the Hamiltonian into two parts due to the presence of the rotation term. It is possible to switch to the rotating Lagrangian coordinates (RLC), a popular method developed by Bao *et al.*, where the rotation term vanishes automatically.[9] This allows utilizing

operator splitting methods or exponential integrators to construct a high order scheme, such as exponential Runge–Kutta methods and Lawson methods for scalar BEC.[14] However, when a real-time dynamics at each time step is on request, one needs to rotate the wave function $\psi_\ell(\mathbf{x}, t)$ from the rotating Lagrangian coordinates to Cartesian coordinates at every time step. Such coordinate switches are quite exhaustive numerically and shall bottleneck the simulation efficiency.

To design high-order compact splitting schemes, the exact integration of linear subproblem is quite crucial. There exists some literature devoted to some particular coordinates or domain. For example, Bao *et al.* proposed a generalized Laguerre–Fourier–Hermite spectral method in the whole space $\mathbb{R}^d$, and they integrate the linear subproblem in polar/cylindrical coordinates.[7] Wang *et al.* introduced a Chebyshev–Fourier spectral method on the bounded disk and integrated the linear subproblem in polar coordinates.[37] Liu *et al.* successfully integrated the *Laplace-rotation-SOC* subproblem exactly in Cartesian coordinates using function-rotation mapping,[26] but it is not optimal in terms of efficiency for non-SOC problems. Recently, Bernier *et al.* proposed an exact integration method in Cartesian coordinates, named as exact splitting method, for the *Laplace-Rotation-Potential* linear subproblem.[12, 13] However, to obtain the splitting coefficients, one has to solve a nonlinear matrix system via an iterative method. Amazingly, we managed to derive an *explicit* formulation for such splitting coefficients by transforming the nonlinear system into a *linear* equation followed by an elaborative block-by-block matrix matching. It is fairly simple and easy to code using such exact and explicit splitting coefficients.

In this paper, we split the CGPEs (1.7) into a linear subproblem

$$i\partial_t \Psi(\mathbf{x}, t) = \left[\left(-\frac{1}{2}\nabla^2 - \Omega L_z\right) I_3 + \mathrm{diag}\{E_1, E_0, E_{-1}\}\right] \Psi(\mathbf{x}, t) := \mathcal{H}_{\mathrm{lin}} \Psi(\mathbf{x}, t), \tag{1.11}$$

and a nonlinear subproblem

$$i\partial_t \Psi(\mathbf{x}, t) = [(V + \beta_n \rho) I_3 + \beta_s \mathbf{F} \cdot \mathbf{f} + \mathbf{B}] \Psi(\mathbf{x}, t) := \mathcal{H}_{\mathrm{non}} \Psi(\mathbf{x}, t). \tag{1.12}$$

Obviously, the linear subproblem is decoupled because each component is independent of the other two and $(-\frac{1}{2}\nabla^2 - \Omega L_z)$ commutes with constant E_ℓ. We derive an explicit exact time integrator for the linear subproblem (1.11) and will refer to it as the *Explicit-Exact-Integrator* (*EEI*) hereafter. In EEI, the wave function is discretized by Fourier spectral method and integrated exactly in phase space. While for the nonlinear subproblem (1.12), we cannot integrate it as usual (see Ref. 35) since the spin vector $\mathbf{F}$ is not conserved in presence of the magnetic field. Here we first derive an exact time-dependent formula of the spin vector, with which the nonlinear subproblem is transformed to a linear one, then we construct explicit high-order schemes using the Magnus integrators.[21, 22] To sum up, each subproblem can be efficiently and accurately solved in either physical or phase space. This compact splitting significantly simplifies the design of high-order schemes.

To sum up, the key advance is that we first design a fast and exact time-splitting scheme for the Laplace-Rotation subproblem with explicit splitting coefficients, which are derived by solving a linear system instead of the nonlinear problem originally proposed in Ref. 12. Explicit coefficients allow for an easy implementation and adaptation to rotating systems. Additionally, for the nonlinear subproblem, we transform it into a linear problem by deriving an exact formula for the time-dependent spin vector, and design explicit high-order schemes.

This paper is organized as follows. In Subsec. 2.1 and 2.2, we propose an EEI for the linear subproblem, and explicit high-order Magnus integrators for the nonlinear subproblem. In Subsec. 2.3, we derive some properties of our numerical method, including mass-conservation (stability), magnetization-conservation, time reversible, time-transverse invariant and rotational symmetry. Detailed spatial/temporal convergence and efficiency tests are presented in Sec. 3, together with some interesting numerical results. Finally, conclusions are drawn in Sec. 4.

2. Compact Splitting Spectral Method

Due to the trapping potential, the wave functions decay to zero exponentially when $|\mathbf{x}| \to \infty$. Therefore, in practical computation, we truncate the problem into a sufficiently large bounded rectangular domain and impose periodic boundary conditions. In this section, we introduce a high-order compact splitting Fourier spectral method for CGPEs (1.1)–(1.4). For simplicity, we shall only present the scheme in 2D and generalization to the 3D case is straightforward. We choose a square domain $\mathbf{R}_L := [-L, L]^2$ and discretize each spatial direction with the same mesh size $h = (2L)/N$ with N being an even positive integer. Define the physical, Fourier index and grid points sets as

$$\begin{aligned}
\mathcal{I}_N &= \{(j,k) \in \mathbb{Z}^2 \,|\, 0 \le j \le N-1, 0 \le k \le N-1\},\\
\mathcal{T}_N &= \{(p,q) \in \mathbb{Z}^2 \,|\, -N/2 \le p \le N/2-1, -N/2 \le q \le N/2-1\},\\
\mathcal{G} &= \{\mathbf{x}_{jk} := (x_j, y_k)^\top := (-L+jh, -L+kh)^\top, (j,k) \in \mathcal{I}_N\},
\end{aligned}$$

and denote $\psi_{\ell,jk}^n$ as the numerical approximation of $\psi_\ell(x_j, y_k, t_n)$ for $(j,k) \in \mathcal{I}_N$.

As stated earlier, the presence of rotation term poses great challenges and a feasible way is to work in the rotating Lagrangian coordinates to eliminate the rotation term.[9] Unfortunately, direct application of RLC faces efficiency bottleneck when coordinates switches are invoked for every time step in some real-time simulation. In our method, we split the Hamiltonian into two parts: the linear operator $\mathcal{H}_{\rm lin}$ (Laplace-Rotation-Zeeman terms), and the nonlinear operator $\mathcal{H}_{\rm non}$. For the linear subproblem, we develop an exact integrator with explicit coefficients. The main idea is to factorize the semigroup, generated by linear part, into products of semigroups, which corresponds to differential operators that can be efficiently approximated using the Fourier spectral method. Further details are provided in Subsec. 2.1. For the nonlinear subproblem, the presence of the magnetic field results

in a time-dependent spin vector, and it makes exact integration very difficult. In fact, we can first derive an exact formula for the spin vector and reduce the nonlinear problem to a linear one. Then we use Magnus integrators to develop efficient high-order schemes, which are to be detailed in Subsec. 2.2.

Specifically, we denote the time sequence as $t_n = n\tau$ with $n = 0, 1, \ldots$ for a given time step $\tau > 0$. The solutions to the linear and nonlinear subproblems from $t = t_n$ are denoted as $\Psi(t) = e^{-i(t-t_n)\mathcal{H}_{\rm lin}}\Psi^n$ and $\Psi(t) = e^{-i(t-t_n)\mathcal{H}_{\rm non}}\Psi^n$, respectively. In practice, high-order splitting methods can be designed as

$$\Psi^{n+1} = \left(\prod_{j=1}^{m} e^{-ia_j\tau\mathcal{H}_{\rm lin}} e^{-ib_j\tau\mathcal{H}_{\rm non}}\right)\Psi^n$$

with the appropriate coefficients $a_j, b_j \in \mathbb{C}$.[38] For the standard second-order Strang splitting, we adopt $m = 2$, $a_1 = a_2 = \frac{1}{2}$ and $b_1 = 1$, $b_2 = 0$, while, fourth-order scheme, proposed by Yoshida, is configured with $m = 4$, $a_1 = a_4 = \frac{1}{2(2-2^{1/3})}$, $a_2 = a_3 = \frac{1-2^{1/3}}{2(2-2^{1/3})}$ and $b_1 = b_3 = \frac{1}{2-2^{1/3}}$, $b_2 = -\frac{2^{1/3}}{2-2^{1/3}}$, $b_4 = 0$.

2.1. *Explicit exact time integrator for linear subproblem*

The exact solution to the following linear problem

$$\begin{cases} i\partial_t\psi_\ell(\mathbf{x},t) = \left[-\dfrac{1}{2}\Delta - \Omega L_z + E_\ell\right]\psi_\ell(\mathbf{x},t), \quad t_n \le t \le t_{n+1}, \\ \psi_\ell(\mathbf{x},t_n) = \psi_\ell^n, \quad \mathbf{x} \in \mathbf{R}_L, \end{cases} \tag{2.1}$$

can be written formally as

$$\psi_\ell(\mathbf{x},t) = e^{i(t-t_n)[\frac{1}{2}\Delta+\Omega L_z - E_\ell]}\psi_\ell^n(\mathbf{x}) = e^{-i(t-t_n)E_\ell}e^{i(t-t_n)[\frac{1}{2}\Delta+\Omega L_z]}\psi_\ell^n(\mathbf{x}). \tag{2.2}$$

To compute $e^{i\tau[\Delta/2+\Omega L_z]}$, we aim to factorize it as a product of sub-operators that can be numerically accessed with great efficiency. Based on the exact splitting method proposed in Refs. 12 and 13, we can factorize it as a product of five sub-operators as follows

$$\boxed{e^{i\tau[\Delta/2+\Omega L_z]} = e^{-i\tau(\zeta_1 x^2+\zeta_2 y^2)}e^{-\tau\xi y\partial_x}e^{i\tau\nabla^\top K\nabla}e^{-\tau\eta x\partial_y}e^{-i\tau\mathbf{x}^\top P\mathbf{x}}} \tag{2.3}$$

with suitable coefficients ζ_1, ζ_2, ξ, $\eta \in \mathbb{R}$ and matrices K, $P \in \mathbb{R}^{2\times 2}$. While for the 3D problem, using Baker–Campbell–Hausdorff (BCH) formula,[29] we can still factorize $e^{i\tau[\Delta/2+\Omega L_z]}$ as a product of five sub-operators instead of seven sub-operators proposed in Refs. 12 and 13. Specifically,

$$\begin{aligned} e^{i\tau[\Delta/2+\Omega L_z]} &= e^{i\tau[\frac{1}{2}\partial_{zz}]}e^{i\tau[\frac{1}{2}\partial_{xx}+\frac{1}{2}\partial_{yy}+\Omega L_z]} \\ &= e^{-i\tau(\zeta_1 x^2+\zeta_2 y^2)}e^{-\tau\xi y\partial_x}e^{i\tau[\nabla_\perp^\top K\nabla_\perp+\frac{1}{2}\partial_{zz}]}e^{-\tau\eta x\partial_y}e^{-i\tau\mathbf{x}_\perp^\top P\mathbf{x}_\perp}, \end{aligned} \tag{2.4}$$

where $\mathbf{x}_\perp = (x, y)^\top$ and $\nabla_\perp = (\partial_x, \partial_y)^\top$.

It appears unlikely to derive explicit formula for such coefficients and matrices, because one has to solve a nonlinear system that involves some complicated matrix exponentials.[12, 13] Fortunately, with an elaborative block-by-block matrix matching technique, we succeeded in turning such nonlinear equations into a series of linear equations, and deriving explicit and exact expressions in the following theorem.

Theorem 2.1. *The coefficients of exact splitting* (2.3) *for* $e^{i\tau[\Delta/2+\Omega L_z]}$ *are given explicitly by*

$$\zeta_1 = \frac{\sec(\Omega\tau)-1}{2\tau^2}, \quad \zeta_2 = \frac{\cos(\Omega\tau)-1}{2\tau^2}, \quad \xi = \frac{\sin(2\Omega\tau)}{2\tau}, \quad \eta = -\frac{\tan(\Omega\tau)}{\tau}, \tag{2.5}$$

$$K = \frac{1}{2}\Theta_{-\tau,\xi} W \Theta_{\tau,\eta}, \quad P = \frac{1}{2\tau^2}\left(W^\top \Theta_{\tau,\xi}\Theta_{\tau,\eta}^\top - I_2\right), \tag{2.6}$$

where $W = \left(\begin{smallmatrix} \cos(\Omega\tau) & \sin(\Omega\tau) \\ -\sin(\Omega\tau) & \cos(\Omega\tau) \end{smallmatrix}\right)$ *is a rotational matrix and* $\Theta_{\tau,v} := \left(\begin{smallmatrix} 1 & \tau v \\ 0 & 1 \end{smallmatrix}\right)$ *with* $v = \xi, \eta$.

Proof. Exact classical-quantum correspondence suggests a way to transform an exact splitting of the differential operators into an exact splitting at the level of the semigroup generated by operators.[1] We rewrite the operator splitting (2.3) as

$$e^{-\tau p^w} = e^{-\tau p_1^w} e^{-\tau p_2^w} e^{-\tau p_3^w} e^{-\tau p_4^w} e^{-\tau p_5^w}, \tag{2.7}$$

where the Weyl quantization is defined as $p_m^w := \mathbf{z}^\top Q_m \mathbf{z}$ with $\mathbf{z} = (\mathbf{x}^\top, -i\nabla^\top)^\top$. To be specific,

$$p^w = -i(\Delta/2 + \Omega L_z) = \mathbf{z}^\top \frac{i}{2}\begin{pmatrix} 0 & A^\top \\ A & I_2 \end{pmatrix}\mathbf{z} := \mathbf{z}^\top Q \mathbf{z} \quad \text{with } A = \begin{pmatrix} 0 & \Omega \\ -\Omega & 0 \end{pmatrix},$$

$$p_1^w = i(\zeta_1 x^2 + \zeta_2 y^2) = \mathbf{z}^\top i \begin{pmatrix} D & 0 \\ 0 & 0 \end{pmatrix}\mathbf{z} := \mathbf{z}^\top Q_1 \mathbf{z} \quad \text{with } D = \begin{pmatrix} \zeta_1 & 0 \\ 0 & \zeta_2 \end{pmatrix},$$

$$p_2^w = \xi y \partial_x = \mathbf{z}^\top \frac{i}{2}\begin{pmatrix} 0 & M_\xi^\top \\ M_\xi & 0 \end{pmatrix}\mathbf{z} := \mathbf{z}^\top Q_2 \mathbf{z} \quad \text{with } M_\xi = \begin{pmatrix} 0 & \xi \\ 0 & 0 \end{pmatrix},$$

$$p_3^w = -i\nabla^\top K \nabla = \mathbf{z}^\top i \begin{pmatrix} 0 & 0 \\ 0 & K \end{pmatrix}\mathbf{z} := \mathbf{z}^\top Q_3 \mathbf{z},$$

$$p_4^w = \eta x \partial_y = \mathbf{z}^\top \frac{i}{2}\begin{pmatrix} 0 & M_\eta \\ M_\eta^\top & 0 \end{pmatrix}\mathbf{z} := \mathbf{z}^\top Q_4 \mathbf{z} \quad \text{with } M_\eta = \begin{pmatrix} 0 & \eta \\ 0 & 0 \end{pmatrix},$$

$$p_5^w = i\mathbf{x}^\top P \mathbf{x} = \mathbf{z}^\top i \begin{pmatrix} P & 0 \\ 0 & 0 \end{pmatrix}\mathbf{z} := \mathbf{z}^\top Q_5 \mathbf{z}.$$

Using exact classical-quantum correspondence, we only need to prove that

$$e^{-2i\tau J_4 Q} = e^{-2i\tau J_4 Q_1} e^{-2i\tau J_4 Q_2} e^{-2i\tau J_4 Q_3} e^{-2i\tau J_4 Q_4} e^{-2i\tau J_4 Q_5}, \tag{2.8}$$

where J_4 is the fundamental symplectic matrix, i.e. $J_4 := \left(\begin{smallmatrix} 0 & I_2 \\ -I_2 & 0 \end{smallmatrix}\right)$ with I_2 being the 2×2 identity matrix. Then, we calculate (2.8) explicitly as follows

$$\begin{aligned}
\begin{pmatrix} W & \tau W \\ 0 & W \end{pmatrix} &= \begin{pmatrix} I_2 & 0 \\ -2\tau D & I_2 \end{pmatrix} \\
&\quad \times \begin{pmatrix} \Theta_{\tau,\xi} & 0 \\ 0 & \Theta_{-\tau,\xi}^{\top} \end{pmatrix} \begin{pmatrix} I_2 & 2\tau K \\ 0 & I_2 \end{pmatrix} \begin{pmatrix} \Theta_{\tau,\eta}^{\top} & 0 \\ 0 & \Theta_{-\tau,\eta} \end{pmatrix} \begin{pmatrix} I_2 & 0 \\ -2\tau P & I_2 \end{pmatrix} \\
&= \begin{pmatrix} \Theta_{\tau,\xi}\Theta_{\tau,\eta}^{\top} - 2\tau G_{12} P & 2\tau \Theta_{\tau,\xi} K \Theta_{-\tau,\eta} \\ -2\tau D \Theta_{\tau,\xi}\Theta_{\tau,\eta}^{\top} - 2\tau G_{22} P & -2\tau D G_{12} + \Theta_{-\tau,\xi}^{\top}\Theta_{-\tau,\eta} \end{pmatrix} \\
&:= \begin{pmatrix} G_{11} & G_{12} \\ G_{21} & G_{22} \end{pmatrix}.
\end{aligned}$$

At first glance, the above equation appears to be a complicated *nonlinear* system. In fact, we can calculate these coefficients exactly by solving a *linear* system using an elaborative block-by-block matching. Starting from the fact that $G_{22} = W$, we calculate ζ_1, η, ζ_2 and ξ sequentially by solving a linear system. Then, we directly compute K and P by matrix inversion for $G_{11} = W$ and $G_{12} = \tau W$. Finally, we need to verify $G_{21} = 0$ with these coefficients.

Specifically, using $G_{22} = -2\tau D G_{12} + \Theta_{-\tau,\xi}^{\top}\Theta_{-\tau,\eta} = W$, we obtain

$$\begin{cases} 1 - 2\tau^2\zeta_1 \cos(\Omega\tau) = \cos(\Omega\tau), \quad \tau\eta - 2\tau^2\zeta_1 \sin(\Omega\tau) = \sin(\Omega\tau), \\ -\tau\xi + 2\tau^2\zeta_2 \sin(\Omega\tau) = -\sin(\Omega\tau), \quad \tau^2\xi\eta + 1 - 2\tau^2\zeta_2 \cos(\Omega\tau) = \cos(\Omega\tau). \end{cases}$$

Solving the above system, we derive the formulas for ζ_1, ζ_2, ξ and η, as shown in (2.5). Then, using

$$G_{12} = 2\tau \Theta_{\tau,\xi} K \Theta_{-\tau,\eta} = \tau W, \quad G_{11} = \Theta_{\tau,\xi}\Theta_{\tau,\eta}^{\top} - 2\tau G_{12} P = W,$$

we have

$$\begin{aligned}
K &= \frac{1}{2}\Theta_{\tau,\xi}^{-1} W \Theta_{-\tau,\eta}^{-1} = \frac{1}{2}\Theta_{-\tau,\xi} W \Theta_{\tau,\eta}, \\
P &= \frac{1}{2\tau^2} W^{-1}(\Theta_{\tau,\xi}\Theta_{\tau,\eta}^{\top} - W) = \frac{1}{2\tau^2}(W^{\top}\Theta_{\tau,\xi}\Theta_{\tau,\eta}^{\top} - I_2).
\end{aligned}$$

Using these coefficients and $G_{22} = W$, we have

$$(2\tau^2 D + I_2)\Theta_{\tau,\xi}\Theta_{\tau,\eta}^{\top} = W.$$

Then, a simple calculation shows that

$$G_{21} = -2\tau D\Theta_{\tau,\xi}\Theta_{\tau,\eta}^{\top} - 2\tau W\left[\frac{1}{2\tau^2}\left(W^{\top}\Theta_{\tau,\xi}\Theta_{\tau,\eta}^{\top} - I_2\right)\right]$$
$$= -\frac{1}{\tau}(2\tau^2 D + I_2)\Theta_{\tau,\xi}\Theta_{\tau,\eta}^{\top} + \frac{1}{\tau}W = -\frac{1}{\tau}W + \frac{1}{\tau}W = 0.$$

The proof is completed. □

The sub-operators in (2.3) or (2.4) can be well approximated by Fourier spectral method with great efficiency thanks to FFT/iFFT.[32] To be specific, the spectral approximations of wave function ψ_ℓ for $d = 2$ in the x- and y- directions are such that

$$\psi_\ell(x,y) \approx \sum_{p=-N/2}^{N/2-1} (\widehat{\psi}_\ell^y)_p e^{i\nu_p^x(x+L)}, \quad \psi_\ell(x,y) \approx \sum_{q=-N/2}^{N/2-1} (\widehat{\psi}_\ell^x)_q e^{i\nu_q^y(y+L)}, \tag{2.9}$$

where $\nu_p^x = (2\pi p)/(2L)$, $\nu_q^y = (2\pi q)/(2L)$. The Fourier coefficients in the x- and y-directions are given as follows

$$(\widehat{\psi}_\ell^y)_p = \frac{1}{N}\sum_{j=0}^{N-1} \psi_\ell(x_j,y)e^{-i\nu_p^x(x_j+L)}, \quad (\widehat{\psi}_\ell^x)_q = \frac{1}{N}\sum_{k=0}^{N-1} \psi_\ell(x,y_k)e^{-i\nu_q^y(y_k+L)}. \tag{2.10}$$

The scheme (2.3) is then discretized as follows

$$\begin{aligned}
\psi_{\ell,jk}^{(1)} &= e^{-i\tau \mathbf{x}_{jk}^{\top} P \mathbf{x}_{jk}}\ \psi_{\ell,jk}^{n},\\
\psi_{\ell,jq}^{(2)} &= e^{-i\tau\eta x_j \nu_q^y}\widehat{(\psi_{\ell,j}^{(1)})}_q,\\
\psi_{\ell,pq}^{(3)} &= e^{-i\tau \boldsymbol{\nu}_{pq}^{\top} K \boldsymbol{\nu}_{pq}}\ \widehat{(\psi_{\ell,q}^{(2)})}_p,\\
\psi_{\ell,pk}^{(4)} &= e^{-i\tau\xi y_k \nu_p^x}\sum_{q=-N/2}^{N/2-1} \psi_{\ell,pq}^{(3)} e^{i\nu_q^y(y_k+L)},\\
\psi_{\ell,jk}^{(n+1)} &= e^{-i\tau(E_\ell+\zeta_1 x_j^2+\zeta_2 y_k^2)}\sum_{p=-N/2}^{N/2-1} \psi_{\ell,pk}^{(4)} e^{i\nu_p^x(x_j+L)}
\end{aligned} \tag{2.11}$$

with $\boldsymbol{\nu}_{pq} = (\nu_p^x, \nu_q^y)^{\top}$.

Remark 2.1. (Efficiency) The coefficients $\zeta_1, \zeta_2, \xi, \eta, K$ and P depend only on the time step τ and the rotation speed Ω, and they can be computed once for all in the pre-computation step. As for the computational costs, the scheme (2.11) requires only $\boldsymbol{dN^{d-1}}$ pairs of *one-dimensional* FFT and iFFT, and the complexity is $\mathcal{O}(N^d \log(N))$.

2.2. *Magnus integrators for nonlinear subproblem*

In this subsection, we introduce explicit high-order schemes to solve

$$\begin{cases} i\partial_t \Psi(\mathbf{x},t) = [(V+\beta_n\rho)I_3 + \beta_s \mathbf{F}\cdot\mathbf{f} + \mathbf{B}]\Psi(\mathbf{x},t) := \mathcal{H}_{\rm non}\Psi(\mathbf{x},t), \\ \Psi(\mathbf{x},t_n) = \Psi^n, \quad \mathbf{x}\in\mathbf{R}_L, \quad t_n \le t \le t_{n+1}. \end{cases} \tag{2.12}$$

It is easy to verify that the density ρ is independent of time, i.e. $\rho(\mathbf{x},t) \equiv \rho(\mathbf{x},t_n) := \rho^n$, $t_n \le t \le t_{n+1}$. Noticing the facts that $f_\nu(\nu = x,y,z)$ are Hermitian matrices and satisfy the commutator relations $[f_x,f_y] := f_xf_y - f_yf_x = if_z$, $[f_y,f_z] = if_x$, $[f_z,f_x] = if_y$, we obtain

$$\begin{aligned} \partial_t F_\nu &= \partial_t(\Psi^{\mathsf{H}} f_\nu \Psi) = i\Psi^{\mathsf{H}}\mathcal{H}_{\rm non} f_\nu \Psi - i\Psi^{\mathsf{H}} f_\nu \mathcal{H}_{\rm non}\Psi \\ &= i\beta_s \Psi^{\mathsf{H}}[\mathbf{F}\cdot\mathbf{f}, f_\nu]\Psi + i\Psi^{\mathsf{H}}[\mathbf{B}, f_\nu]\Psi \\ &= i\beta_s(F_x\Psi^{\mathsf{H}}[f_x,f_\nu]\Psi + F_y\Psi^{\mathsf{H}}[f_y,f_\nu]\Psi + F_z\Psi^{\mathsf{H}}[f_z,f_\nu]\Psi) + i\Psi^{\mathsf{H}}[\mathbf{B},f_\nu]\Psi \\ &= i\Psi^{\mathsf{H}}[\mathbf{B},f_\nu]\Psi, \quad \nu = x,y,z. \end{aligned}$$

Using the relation $\mathbf{B} = \sqrt{2}Bf_x$, we have

$$\partial_t F_x = 0, \quad \partial_t F_y = -\sqrt{2}BF_z, \quad \partial_t F_z = \sqrt{2}BF_y, \tag{2.13}$$

from which we derive exact and explicit formula for the spin vector $\mathbf{F}(t)$ as follows

$$\begin{pmatrix} F_y(t) \\ F_z(t) \end{pmatrix} = \begin{pmatrix} \cos(\sqrt{2}B(t-t_n)) & -\sin(\sqrt{2}B(t-t_n)) \\ \sin(\sqrt{2}B(t-t_n)) & \cos(\sqrt{2}B(t-t_n)) \end{pmatrix} \begin{pmatrix} F_y^n \\ F_z^n \end{pmatrix}, \quad F_x(t) \equiv F_x^n.$$

Clearly, we can see that the seemingly nonlinear operator $\mathcal{H}_{\rm non}$ actually depends on only time variable t, therefore, the nonlinear system (2.12) is in fact a *linear* system. We use Magnus integrators (see Ref. 22) to design an explicit high-order solver for this system (2.12). The idea is to write the solution in the following form:

$$\Psi^{n+1}(\mathbf{x}) = e^{-i\Omega_n(\tau)}\Psi^n(\mathbf{x}), \quad \Omega_n(\tau) \in \mathbb{C}^{d\times d}. \tag{2.14}$$

We give specific expressions for $\Omega_n(\tau)$ associated with the second-order and fourth-order integrators, respectively, and other high-order integrators can be obtained in a similar manner.[22] That is,

- **Second-order**: The matrix $\Omega_n(\tau)$ reads as

$$\Omega_n(\tau) = \int_0^\tau \mathcal{H}_{\rm non}(t_n+\sigma)\mathrm{d}\sigma. \tag{2.15}$$

- **Fourth-order**: The matrix $\Omega_n(\tau)$ reads as

$$\begin{aligned} \Omega_n(\tau) = &\int_0^\tau \mathcal{H}_{\rm non}(t_n+\sigma)\mathrm{d}\sigma \\ &+ \frac{1}{2}i\int_0^\tau \left[\int_0^\sigma \mathcal{H}_{\rm non}(t_n+\mu)\mathrm{d}\mu, \mathcal{H}_{\rm non}(t_n+\sigma)\right]\mathrm{d}\sigma. \end{aligned} \tag{2.16}$$

Fortunately, integrals in (2.15) and (2.16) can both be computed exactly. To be specific, we obtain the second-order integrator of ODEs (2.12) as

$$\Psi^{n+1}(\mathbf{x}) = e^{-i\Omega_n(\tau)}\Psi^n(\mathbf{x}) = e^{-i\tau(V+\beta_n\rho^n)}e^{-i\int_0^\tau \beta_s\mathbf{F}(t_n+\sigma)\cdot\mathbf{f}+\mathbf{B}\,\mathrm{d}\sigma}\Psi^n(\mathbf{x})$$
$$:= e^{-i\tau(V+\beta_n\rho^n)}e^{-i\mathbf{S}_{2\mathrm{nd}}}\Psi^n(\mathbf{x}), \tag{2.17}$$

where $\mathbf{S}_{2\mathrm{nd}}$, a Hermitian matrix, is given explicitly as follows:

$$\mathbf{S}_{2\mathrm{nd}} := \int_0^\tau \beta_s\mathbf{F}(t_n+\sigma)\cdot\mathbf{f}+\mathbf{B}\,\mathrm{d}\sigma = \begin{pmatrix}\beta & \alpha & 0\\ \overline{\alpha} & 0 & \alpha\\ 0 & \overline{\alpha} & -\beta\end{pmatrix}, \tag{2.18}$$

with matrix entries

$$\alpha = -\frac{i\beta_s}{2B}[\sin(\sqrt{2}B\tau)F_y^n + (\cos(\sqrt{2}B\tau)-1)F_z^n] + \tau\left(\frac{\beta_s}{\sqrt{2}}F_x^n + B\right), \tag{2.19}$$

$$\beta = \frac{\beta_s}{\sqrt{2}B}[(1-\cos(\sqrt{2}B\tau))F_y^n + \sin(\sqrt{2}B\tau)F_z^n]. \tag{2.20}$$

Since $\mathbf{S}_{2\mathrm{nd}}$ is Hermitian, it can be diagonalized as $\mathbf{S}_{2\mathrm{nd}} = U\Lambda U^{\mathsf{H}}$, where unitary matrix U and real diagonal matrix Λ read as

$$U = \frac{1}{\lambda}\begin{pmatrix}-\alpha & -\dfrac{\alpha|\alpha|}{\beta-\lambda} & \dfrac{\alpha|\alpha|}{\beta+\lambda}\\ \beta & |\alpha| & -|\alpha|\\ \overline{\alpha} & \dfrac{\overline{\alpha}|\alpha|}{\beta+\lambda} & -\dfrac{\overline{\alpha}|\alpha|}{\beta-\lambda}\end{pmatrix}, \quad \Lambda = \begin{pmatrix}0 & 0 & 0\\ 0 & \lambda & 0\\ 0 & 0 & -\lambda\end{pmatrix}, \quad \lambda = \sqrt{\beta^2+2|\alpha|^2}.$$

Hence, $e^{-i\mathbf{S}_{2\mathrm{nd}}}$ can be computed analytically as

$$e^{-i\mathbf{S}_{2\mathrm{nd}}} = Ue^{-i\Lambda}U^{\mathsf{H}} = \begin{pmatrix}g_{11} & g_{12} & g_{13}\\ g_{21} & g_{22} & -\overline{g}_{21}\\ \overline{g}_{13} & -\overline{g}_{12} & \overline{g}_{11}\end{pmatrix} := \mathbf{G}_{2\mathrm{nd}}, \tag{2.21}$$

where

$$g_{11} = \frac{1}{\lambda^2}\left[|\alpha|^2 + \frac{1}{4}q_1(\beta^2+\lambda^2) + \frac{1}{2}q_2\beta\lambda\right], \quad g_{12} = \alpha c_0, \quad g_{13} = \frac{\alpha^2}{2\lambda^2}(q_1-2),$$

$$g_{22} = \frac{1}{\lambda^2}[\beta^2 + |\alpha|^2 q_1], \quad g_{21} = \overline{\alpha}c_0, \quad c_0 = \frac{1}{2\lambda^2}[\beta(q_1-2)+\lambda q_2]$$

with $q_1 = 2\cos(\lambda)$ and $q_2 = -2i\sin(\lambda)$. Therefore, we can obtain an explicit second-order integrator for the subproblem (2.12), i.e.

$$\boxed{\Psi^{n+1}(\mathbf{x}) = e^{-i\tau(V+\beta_n\rho^n)}\ \mathbf{G}_{2\mathrm{nd}}\ \Psi^n(\mathbf{x}).} \tag{2.22}$$

Remark 2.2. (Non-magnetic field) The integrator (2.22) is *exact* when the magnetic field disappears (i.e. $B = 0$), because $\partial_t F_\nu = 0$ for $\nu = x, y, z$, which implies

$\mathcal{H}_{\rm non}(\Psi) = \mathcal{H}_{\rm non}(\Psi^n)$. When B goes to zero, the matrix entries (2.19)–(2.20) tends to $\alpha = \frac{1}{\sqrt{2}}\tau\beta_s F_-^n$ and $\beta = \tau\beta_s F_z^n$.

Remark 2.3. (Fourth-order integrator) The fourth-order integrator for the subproblem (2.12) reads as

$$\boxed{\Psi^{n+1}(\mathbf{x}) = e^{-i\tau(V+\beta_n\rho^n)}\ \mathbf{G}_{\rm 4th}\ \Psi^n(\mathbf{x}),} \tag{2.23}$$

where the matrix $\mathbf{G}_{\rm 4th}$ takes the same form as $\mathbf{G}_{\rm 2nd}$ (2.21), and the only modification is to replace α and β in $\mathbf{G}_{\rm 2nd}$ with the expressions given in (A.1) and (A.2). A detailed step-by-step computation can be found in Appendix A. It is worthy to emphasize that other high-order integrators can be constructed in a similar way.

In implementation, from time $t = t_n$ to $t = t_{n+1}$, we combine the solvers (2.11) and (2.22) for linear and nonlinear subproblems via the classical Strang splitting and provide a detailed stepwise algorithm (Algorithm 1).

Algorithm 1. Second-order compact operator splitting spectral method.

Input: Initial data ψ_ℓ^n at time t_n, time step τ.

1. Precompute the coefficients ζ_1, ζ_2, ξ, η, K, P by Eqs. (2.5) and (2.6).
2. Solve linear subproblem by EEI (2.11) for half time step $\tau/2$ with initial data ψ_ℓ^n:
   (i) $\psi_\ell^{(1)} = e^{-i\frac{\tau}{2}\mathbf{x}^\top P\mathbf{x}}\psi_\ell^n$
   (ii) $\psi_\ell^{(2)} = e^{-i\frac{\tau}{2}\eta x\nu^y}\mathcal{F}_y[\psi_\ell^{(1)}]$
   (iii) $\psi_\ell^{(3)} = e^{-i\frac{\tau}{2}\boldsymbol{\nu}^\top K\boldsymbol{\nu}}\mathcal{F}_x[\psi_\ell^{(2)}]$
   (iv) $\psi_\ell^{(4)} = e^{-i\frac{\tau}{2}\xi y\nu^x}\mathcal{F}_y^{-1}[\psi_\ell^{(3)}]$
   (v) $\psi_\ell^* = e^{-i\frac{\tau}{2}(E_\ell+\zeta_1 x^2+\zeta_2 y^2)}\mathcal{F}_x^{-1}[\psi_\ell^{(4)}]$
   Here, $\mathcal{F}_x/\mathcal{F}_x^{-1}$ and $\mathcal{F}_y/\mathcal{F}_y^{-1}$ denote the forward/backward discrete Fourier transform in the x- and y- directions, respectively.
3. Solve nonlinear subproblem by Eq. (2.22) for one step τ beginning with the data ψ_ℓ^* acquired from step 2:
$$\psi_1^{**} = e^{-i\tau(V+\beta_n\rho^n)}(g_{11}\psi_1^* + g_{12}\psi_0^* + g_{13}\psi_{-1}^*)$$
$$\psi_0^{**} = e^{-i\tau(V+\beta_n\rho^n)}(g_{21}\psi_1^* + g_{22}\psi_0^* - \bar{g}_{21}\psi_{-1}^*)$$
$$\psi_{-1}^{**} = e^{-i\tau(V+\beta_n\rho^n)}(\bar{g}_{13}\psi_1^* - \bar{g}_{12}\psi_0^* + \bar{g}_{11}\psi_{-1}^*)$$
4. Solve linear subproblem by repeating steps (i)–(v) in step 2, using initial data ψ_ℓ^{**}, to obtain ψ_ℓ^{n+1}.

Output: Numerical solution ψ_ℓ^{n+1} at time $t_{n+1} = t_n + \tau$.

Remark 2.4. (Arbitrary high-order schemes) Using the EEI method for linear subproblem and the Magnus integrators for nonlinear subproblem, it is simple to construct arbitrary high-order schemes based on high-order operator splitting method.[38]

2.3. *Properties of the numerical scheme*

There are many important dynamical properties for the CGPEs (1.1)–(1.3), and here we mention several important ones that are still valid with our method on discrete level. In this subsection, we derive the properties of our numerical method, including the mass-conservation (stability), magnetization-conservation, time reversible, time-transverse invariant and rotational symmetry. For convenience, we only provide proofs for the 2D case and extension to 3D is simple. We denote the discrete l^2-norm of ψ_ℓ^n as $\|\psi_\ell^n\|_{l^2} = (h^2 \sum_{j=0}^{N-1} \sum_{k=0}^{N-1} |\psi_{\ell,jk}^n|^2)^{\frac{1}{2}}$.

Lemma 2.1. (Mass-conservation) *For any $h, \tau > 0$, the compact splitting Fourier spectral method conserves the total mass on discrete level, i.e.*

$$\sum_{\ell=-1}^{1} \|\psi_\ell^n\|_{l^2}^2 = \sum_{\ell=-1}^{1} \|\psi_\ell^0\|_{l^2}^2. \tag{2.24}$$

In other words, our scheme is unconditionally stable *in l^2-norm.*

Proof. For the nonlinear subproblem (2.14)–(2.16), it is easy to see that $\Omega_n(\tau)$ is a Hermitian matrix, then we have

$$\|\Psi^{n+1}\|_{l^2}^2 = \|e^{-i\Omega_n(\tau)}\Psi^n\|_{l^2}^2 = \|\Psi^n\|_{l^2}^2, \quad \text{where } \|\Psi^n\|_{l^2}^2 := \sum_{\ell=-1}^{1} \|\psi_\ell^n\|_{l^2}^2.$$

While for the linear subproblem (2.11), we have

$$\|\psi_\ell^{(1)}\|_{l^2}^2 = h^2 \sum_{j=0}^{N-1} \sum_{k=0}^{N-1} |e^{-i\tau \mathbf{x}_{jk}^\top P \mathbf{x}_{jk}} \psi_{\ell,jk}^n|^2 = \|\psi_\ell^n\|_{l^2}^2.$$

Using the following identities

$$\sum_{q=-N/2}^{N/2-1} e^{i2\pi jq/N} = \sum_{q=0}^{N-1} e^{i2\pi jq/N} = \begin{cases} 0, & j \neq mN, \\ N, & j = mN, \end{cases} \quad m \in \mathbb{Z}, \tag{2.25}$$

we obtain

$$\begin{aligned} \sum_{j=0}^{N-1} \sum_{q=-N/2}^{N/2-1} |\psi_{\ell,jq}^{(2)}|^2 &= \sum_{j=0}^{N-1} \sum_{q=-N/2}^{N/2-1} |e^{-i\tau\eta x_j \nu_q} \widehat{(\psi_{\ell,j}^{(1)})}_q|^2 \\ &= \frac{1}{N^2} \sum_{j=0}^{N-1} \sum_{q=-N/2}^{N/2-1} \left| \sum_{k=0}^{N-1} \psi_{\ell,jk}^{(1)} e^{i2\pi kq/N} \right|^2 = \frac{1}{N} \sum_{j=0}^{N-1} \sum_{k=0}^{N-1} |\psi_{\ell,jk}^{(1)}|^2. \end{aligned}$$

Similarly, we have

$$\|\psi_\ell^{(n+1)}\|_{l^2}^2 = h^2 \sum_{j=0}^{N-1}\sum_{k=0}^{N-1}\left|\sum_{p=-N/2}^{N/2-1}\psi_{\ell,pk}^{(4)} e^{i\nu_p^x(x_j+L)}\right|^2 = h^2 N \sum_{p=-N/2}^{N/2-1}\sum_{k=0}^{N-1}|\psi_{\ell,pk}^{(4)}|^2$$

$$= h^2 N^2 \sum_{p=-N/2}^{N/2-1}\sum_{q=-N/2}^{N/2-1}|\widehat{(\psi_{\ell,q}^{(2)})}_p|^2 = h^2 N \sum_{j=0}^{N-1}\sum_{q=-N/2}^{N/2-1}|\psi_{\ell,jq}^{(2)}|^2 \tag{2.26}$$

$$= h^2 \sum_{j=0}^{N-1}\sum_{k=0}^{N-1}|\psi_{\ell,jk}^{(1)}|^2 = \|\psi_\ell^{(1)}\|_{l^2}^2, \quad \ell = 1, 0, -1. \tag{2.27}$$

To sum up, we can prove that the following relation

$$\sum_{\ell=-1}^{1}\|\psi_\ell^{n+1}\|_{l^2}^2 = \sum_{\ell=-1}^{1}\|\psi_\ell^{(1)}\|_{l^2}^2 = \sum_{\ell=-1}^{1}\|\psi_\ell^{n}\|_{l^2}^2$$

holds true. □

Lemma 2.2. (Magnetization-conservation) *For any $h, \tau > 0$, the compact splitting Fourier spectral method conserves the magnetization on discrete level, i.e.*

$$\sum_{\ell=-1}^{1}\ell\|\psi_\ell^n\|_{l^2}^2 = \sum_{\ell=-1}^{1}\ell\|\psi_\ell^0\|_{l^2}^2. \tag{2.28}$$

Proof. For the linear subproblem, from the proof of Lemma 2.1, we have

$$\|\psi_1^n\|_{l^2}^2 - \|\psi_{-1}^n\|_{l^2}^2 = \|\psi_1^0\|_{l^2}^2 - \|\psi_{-1}^0\|_{l^2}^2.$$

For the nonlinear subproblem with $B = 0$, we have[35]

$$\Psi^{n+1} = e^{-i(V+\beta_n\rho^n)\tau}\left[\cos(\beta_s\tau|\mathbf{F}^n|)\ \Psi^n - i\frac{\sin(\beta_s\tau|\mathbf{F}^n|)}{|\mathbf{F}^n|}\mathbf{S}(\Psi^n)\Psi^n\right],$$

where $|\mathbf{F}^n| = \sqrt{(F_x^n)^2 + (F_y^n)^2 + (F_z^n)^2}$. A direct calculation shows

$$\begin{aligned}
&|\psi_1^{n+1}|^2 - |\psi_{-1}^{n+1}|^2 \\
&\quad = \cos^2(\beta_s\tau|\mathbf{F}^n|)(|\psi_1^n|^2 - |\psi_{-1}^n|^2) \\
&\qquad + \frac{\sin^2(\beta_s\tau|\mathbf{F}^n|)}{|F^n|^2}\left(\left|F_z^n\psi_1^n + \frac{1}{\sqrt{2}}F_-^n\psi_0^n\right|^2 - \left|\frac{1}{\sqrt{2}}F_+^n\psi_0^n - F_z^n\psi_{-1}^n\right|^2\right) \\
&\quad = \cos^2(\beta_s\tau|\mathbf{F}^n|)(|\psi_1^n|^2 - |\psi_{-1}^n|^2) + \frac{\sin^2(\beta_s\tau|\mathbf{F}^n|)}{|\mathbf{F}^n|^2}|\mathbf{F}^n|^2(|\psi_1^n|^2 - |\psi_{-1}^n|^2) \\
&\quad = |\psi_1^n|^2 - |\psi_{-1}^n|^2,
\end{aligned}$$

which implies $\|\psi_1^{n+1}\|_{l^2}^2 - \|\psi_{-1}^{n+1}\|_{l^2}^2 = \|\psi_1^n\|_{l^2}^2 - \|\psi_{-1}^n\|_{l^2}^2$. We complete the proof. □

Lemma 2.3. (Time reversible) *The compact splitting Fourier spectral method is time reversible, i.e. scheme* (*Algorithm* 1) *remains unchanged if we interchange* $n \leftrightarrow n+1$ *and* $\tau \leftrightarrow -\tau$.

Proof. It is sufficient to demonstrate that the numerical methods to both subproblems satisfy time-reversal property. For the nonlinear subproblem (2.14), we can easily prove that $\Omega_{n+1}(-\tau) = -\Omega_n(\tau)$ holds true for both second-order and fourth-order scheme. Therefore, we have

$$e^{-i\Omega_{n+1}(-\tau)}\Psi^{n+1} = e^{i\Omega_n(\tau)}(e^{-i\Omega_n(\tau)}\Psi^n) = \Psi^n.$$

For the linear subproblem (2.2), the following equation

$$e^{i\tau E_\ell}e^{-i\tau[\Delta/2+\Omega L_z]}\psi_\ell^{n+1} = e^{i\tau E_\ell}e^{-i\tau[\Delta/2+\Omega L_z]}[e^{-i\tau E_\ell}e^{i\tau[\Delta/2+\Omega L_z]}\psi_\ell^n] = \psi_\ell^n,$$

holds evidently. The proof is completed. □

Lemma 2.4. (Time-transverse invariant) *If a constant* C *is added to the external potential* $V(\mathbf{x})$, *i.e.* $V(\mathbf{x}) \to V(\mathbf{x})+C$, *then the discrete wave function* Ψ_{jk}^n *obtained from Algorithm* 1 *shall get multiplied by a phase factor* $e^{-in\tau C}$. *That is,*

$$\Psi_{jk}^n \to e^{-in\tau C}\Psi_{jk}^n.$$

Proof. Let Ψ_{jk}^n and $\widetilde{\Psi}_{jk}^n$ be the wave function obtained by Algorithm 1 with potential V and $V+C$, respectively. Then, we have

$$\begin{aligned}
\widetilde{\Psi}^1 &= e^{-i[V+C+\beta_n\rho^n]\tau}\mathbf{G}_{2\mathrm{nd}}\Psi^0 = e^{-i\tau C}\Psi^1,\\
\widetilde{\Psi}^2 &= e^{-i[V+C+\beta_n\rho^n]\tau}\mathbf{G}_{2\mathrm{nd}}\Psi^1 = e^{-i2\tau C}\Psi^2,\\
&\cdots\\
\widetilde{\Psi}^n &= e^{-i[V+C+\beta_n\rho^n]\tau}\mathbf{G}_{2\mathrm{nd}}\Psi^n = e^{-in\tau C}\Psi^n.
\end{aligned}$$

The proof is completed. □

The rotating spin-1 CGPE (1.1)–(1.3) keeps *rotational symmetry* when the trapping potential $V(\mathbf{x})$ is radially symmetric. To be precise, for solutions starting with initial value $\psi_\ell^0(\mathbf{x})$ and $\widetilde{\psi}_\ell^0(\mathbf{x}) = \psi_\ell^0(R(\theta)\mathbf{x})$, $\widetilde{\psi}_\ell(\mathbf{x},t)$ is also the θ-rotation of $\psi_\ell(\mathbf{x},t)$ at time t, i.e. $\widetilde{\psi}_\ell(\mathbf{x},t) = \psi_\ell(R(\theta)\mathbf{x},t)$, where $R(\theta) = \left(\begin{smallmatrix}\cos(\theta) & \sin(\theta)\\ -\sin(\theta) & \cos(\theta)\end{smallmatrix}\right)$ is the rotational matrix. In other words, the system will keep the same rotational symmetry as the initial wave function, e.g. $\psi(\mathbf{x},t)$ is $\boldsymbol{\theta}$*-rotational symmetric* at any time t if $\psi_0(\mathbf{x})$ is θ-rotational symmetric.

Lemma 2.5. (Rotational symmetry) *For rotating spin-*1 *CGPE* (1.1)–(1.3) *with radially symmetric potential, i.e.* $V(\mathbf{x}) = V(|\mathbf{x}|)$, *the semi-discrete scheme keeps rotational symmetry.*

Proof. To confirm the rotational symmetry, it suffices to prove that

$$\widetilde{\psi}_\ell^{n+1}(\mathbf{x}) = \psi_\ell^{n+1}(R(\theta)\mathbf{x})$$

if $\widetilde{\psi}_\ell^n(\mathbf{x}) = \psi_\ell^n(R(\theta)\mathbf{x})$. For simplicity, we shall denote $\widetilde{\mathbf{x}} = R(\theta)\mathbf{x}$. As shown before, the numerical solution to the nonlinear subproblem (2.12) reads explicitly as

$$\begin{aligned}\widetilde{\Psi}^{n+1}(\mathbf{x}) &= e^{-i\tau(V(\mathbf{x})+\beta_n\widetilde{\rho}^n(\mathbf{x}))}\mathbf{G}_{2\mathrm{nd}}(\widetilde{\Psi}^n(\mathbf{x}))\widetilde{\Psi}^n(\mathbf{x})\\ &= e^{-i\tau(V(\widetilde{\mathbf{x}})+\beta_n\rho^n(\widetilde{\mathbf{x}}))}\mathbf{G}_{2\mathrm{nd}}(\Psi^n(\widetilde{\mathbf{x}}))\Psi^n(\widetilde{\mathbf{x}})\\ &= \Psi^{n+1}(\widetilde{\mathbf{x}}) = \Psi^{n+1}(R(\theta)\mathbf{x}).\end{aligned}$$

While for the linear subproblem (2.1), using chain rule, we obtain

$$\Delta\widetilde{\psi}_\ell^n(\mathbf{x}) = \Delta_{\widetilde{\mathbf{x}}}\psi_\ell^n(\widetilde{\mathbf{x}}), \quad L_z\widetilde{\psi}_\ell^n(\mathbf{x}) = L_{\tilde{z}}\psi_\ell^n(\widetilde{\mathbf{x}})$$

and

$$\begin{aligned}\widetilde{\psi}_\ell^{n+1}(\mathbf{x}) &= e^{i\tau[\frac{1}{2}\Delta+\Omega L_z-E_\ell]}\widetilde{\psi}_\ell^n(\mathbf{x}) = e^{i\tau[\frac{1}{2}\Delta_{\widetilde{\mathbf{x}}}+\Omega L_{\tilde{z}}-E_\ell]}\psi_\ell^n(\widetilde{\mathbf{x}})\\ &= \psi_\ell^{n+1}(\widetilde{\mathbf{x}}) = \psi_\ell^{n+1}(R(\theta)\mathbf{x}).\end{aligned}$$

Therefore, we can conclude that the semi-discrete scheme keeps rotational symmetry. □

3. Numerical Results

In this section, we first test the accuracies and efficiency in spatial and temporal directions. Then we study the dynamical properties, including energy, mass and magnetization conservation, evolution of angular momentum expectation and condensate widths, and carry out a comparison on the rotational symmetry conservation with some existing numerical methods. Finally, we utilize our method to study various interesting phenomena, such as the evolution of quantized vortices and dynamics of BEC under honeycomb potential.

3.1. *Accuracy confirmation*

In this subsection, we test the temporal and spatial convergence for both 2D and 3D cases. For simplicity, we denote the second-order/fourth-order compact splitting as **CS2**/**CS4**. The numerical error is measured in following norm

$$e_\ell^{h,\tau}(t) := \|\psi_\ell^{\mathrm{ref}}(t) - \psi_\ell^{(h,\tau)}(t)\|_{l^2}/\|\psi_\ell^{\mathrm{ref}}(t)\|_{l^2}, \quad \ell = 1, 0, -1,$$

where $\psi_\ell^{(h,\tau)}(t)$ is the numerical approximation at time t obtained with the mesh size h and time step τ, and $\psi_\ell^{\mathrm{ref}}(t)$ is the reference solution at time t. In our simulations, unless otherwise specified, we choose computational domain $\mathbf{R}_L = [-16, 16]^d$, mesh size $h = 1/8$, time step $\tau = 10^{-4}$. The harmonic potential is taken as $V(\mathbf{x}) = |\mathbf{x}|^2/2$.

Example 1. (Linear case) We test the temporal accuracy for linear subproblem solver EEI (2.11). To this end, we choose $h = 1/4$, $\tau = 1$, $E_\ell = 0$ and consider the following non-radially symmetric initial data

$$\psi_\ell^0(\mathbf{x}) = \frac{1}{\pi^{1/4}}x^2e^{-\frac{1}{2}|\mathbf{x}|^2}.$$

Table 1. Temporal discretization errors $e_\ell^{h,\tau}$ $(\ell = 1, 0, -1)$ of the EEI method in Example 1.

Ω	0.2	0.4	0.8
2D	6.2005E-16	4.7358E-16	4.6741E-16
3D	5.7673E-16	6.3983E-16	5.8956E-16

The exact solution is given explicitly as[9, 25]

$$\psi_\ell(\mathbf{x}, t) = \frac{1}{\pi^{1/4}} \frac{(\cos(\Omega t)x - \sin(\Omega t)y)^2 - t^2 + it}{(1+it)^{(d+4)/2}} e^{-\frac{1}{2(it+1)}|\mathbf{x}|^2},$$

and the detailed derivation are provided in Appendix B.

Table 1 lists the temporal errors of EEI method at time $t = 1$ with different Ω, from which one can see that the EEI method is *exact* in time.

Example 2. (Nonlinear case) We verify the spectral accuracy in space and high-order temporal convergence for both 2D and 3D cases. To this end, we choose $\Omega = 0.2$, $E_\ell = 1$ and the following parameters

- **2D case**: $\beta_n = 100, \beta_s = -1, B = 2$, and the initial data

$$\psi_1^0(\mathbf{x}) = (x+iy)\phi(\mathbf{x}), \quad \psi_0^0(\mathbf{x}) = 2\phi(\mathbf{x}), \quad \psi_{-1}^0(\mathbf{x}) = (x+2iy)\phi(\mathbf{x}) \tag{3.1}$$

  with $\phi(\mathbf{x}) = \sqrt{2/(15\pi)}e^{-|\mathbf{x}|^2/2}$.
- **3D case**: $\beta_n = 10, \beta_s = 1, B = 1$, and the initial data

$$\psi_1^0(\mathbf{x}) = \phi(\mathbf{x}), \quad \psi_0^0(\mathbf{x}) = 3\sqrt{2}\phi(\mathbf{x}), \quad \psi_{-1}^0(\mathbf{x}) = \phi(\mathbf{x})$$

  with $\phi(\mathbf{x}) = \sqrt{0.05}/\pi^{3/4}(x+iy)e^{-|\mathbf{x}|^2/2}$.

To confirm the convergence of CS2/CS4, let ψ_ℓ^{ref} be the numerical reference solution obtained by CS2/CS4 with very fine mesh size $h_0 = \frac{1}{2^{7-d}}$ and small time step $\tau_0 = 10^{-4}$. To calculate the spatial errors, we always use time step τ_0 so that the errors from temporal discretization can be neglected compared to those from spatial discretization. Similarly, the temporal errors are obtained when mesh size h_0 is used.

We take the computational domain $\mathbf{R}_L = [-12, 12]^2$ in 2D and $[-8, 8]^3$ in 3D. Table 2 lists the temporal and spatial errors of CS2 and CS4 at time $t = 0.5$ for the 2D problem, while Table 3 lists those at time $t = 0.3$ for the 3D case. From these tables, one can see the spatial *spectrally* accuracy and *second/fourth* order temporal convergence in CS2/CS4.

3.2. *Efficiency test*

To show the efficiency performance of our method, we investigate the computational costs, measured in CPU time, as a function of the total grid points.

Example 3. (Efficiency) We test the efficiency by showing the computational time variation versus the total grid number $N_{\text{tot}} := N^d$. The parameters are chosen the

Table 2. Numerical errors of CS2 and CS4 at time $t = 0.5$ for 2D case in Example 2.

CS2			*Temporal* direction		
	τ	1/80	1/160	1/320	1/640
	$e_1^{h_0,\tau}$	3.8009E-04	9.4930E-05	2.3727E-05	5.9313E-06
	rate		2.0014	2.0003	2.0001
	$e_0^{h_0,\tau}$	3.6387E-04	9.0816E-05	2.2695E-05	5.6731E-06
	rate		2.0024	2.0006	2.0001
	$e_{-1}^{h_0,\tau}$	3.7662E-04	9.4058E-05	2.3508E-05	5.8767E-06
	rate		2.0015	2.0004	2.0001
			Spatial direction		
	h	1/2	1/4	1/8	1/16
	e_1^{h,τ_0}	6.4844E-02	1.8722E-04	1.5849E-09	6.8645E-13
	e_0^{h,τ_0}	7.4716E-02	2.5605E-04	1.1263E-09	6.1212E-13
	e_{-1}^{h,τ_0}	6.4912E-02	1.8862E-04	1.5153E-09	6.3363E-13
CS4			*Temporal* direction		
	τ	1/80	1/160	1/320	1/640
	$e_1^{h_0,\tau}$	7.0278E-06	4.3518E-07	2.7137E-08	1.6951E-09
	rate		4.0134	4.0033	4.0008
	$e_0^{h_0,\tau}$	9.1809E-06	5.6785E-07	3.5400E-08	2.2110E-09
	rate		4.0150	4.0037	4.0010
	$e_{-1}^{h_0,\tau}$	7.4004E-06	4.5812E-07	2.8565E-08	1.7834E-09
	rate		4.0138	4.0034	4.0008
			Spatial direction		
	h	1/2	1/4	1/8	1/16
	e_1^{h,τ_0}	6.4844E-02	1.8722E-04	1.5849E-09	1.6546E-12
	e_0^{h,τ_0}	7.4716E-02	2.5605E-04	1.1260E-09	1.3798E-12
	e_{-1}^{h,τ_0}	6.4912E-02	1.8862E-04	1.5153E-09	1.5307E-12

same as in Example 2. The algorithms were implemented in FORTRAN, and run on a single 2.30GH Intel(R) Xeon(R) Sliver 4316 CPU with a 30 MB cache in Ubuntu GNU/Linux with the Intel complier ifort.

Figure 1 displays log–log plot of timing results for CS2/CS4, elapsed from time $t = 0$ to $t = 0.1$ with time step $\tau = 10^{-3}$, versus the total grid number N_{tot} in both 2D and 3D cases. From Fig. 1, we can see that our method is efficient and the CPU time scales roughly as $CN_{\text{tot}} \log(N_{\text{tot}})$, which agrees well with our theoretical analysis (Remark 2.1).

Example 4. (Efficiency comparison) Here, we compare our method with the one proposed in Refs. 11 and 36, where they proposed a second-order scheme by splitting the Hamiltonian into three parts and applying the ADI technique to handle the Laplace-Rotation linear subproblem. For convenience, we denote this method as *ADI2*. However, it is somewhat tedious to construct high-order schemes with such three parts. For comparison, we develop a fourth-order scheme based on the Yoshida

Table 3. Numerical errors of CS2 and CS4 at time $t = 0.3$ for 3D case in Example 2.

CS2			*Temporal* direction		
	τ	1/40	1/80	1/160	1/320
	$e_1^{h_0,\tau}$	5.5530E-05	1.3867E-05	3.4658E-06	8.6640E-07
	rate		2.0016	2.0004	2.0001
	$e_0^{h_0,\tau}$	5.4062E-05	1.3501E-05	3.3745E-06	8.4357E-07
	rate		2.0015	2.0004	2.0001
	$e_{-1}^{h_0,\tau}$	5.5530E-05	1.3867E-05	3.4658E-06	8.6640E-07
	rate		2.0016	2.0004	2.0001
			Spatial direction		
	h	1	1/2	1/4	1/8
	e_1^{h,τ_0}	2.2153E-02	4.9362E-04	2.8204E-08	4.7221E-13
	e_0^{h,τ_0}	2.1108E-02	4.6762E-04	2.5627E-08	4.6931E-13
	e_{-1}^{h,τ_0}	2.2153E-02	4.9362E-04	2.8204E-08	4.7256E-13
CS4			*Temporal* direction		
	τ	1/20	1/40	1/80	1/160
	$e_1^{h_0,\tau}$	2.6965E-06	1.6438E-07	1.0223E-08	6.3828E-10
	rate		4.0360	4.0071	4.0015
	$e_0^{h_0,\tau}$	2.5321E-06	1.5431E-07	9.5966E-08	5.9912E-10
	rate		4.0364	4.0072	4.0016
	$e_{-1}^{h_0,\tau}$	2.6965E-06	1.6438E-07	1.0223E-08	6.3828E-10
	rate		4.0360	4.0071	4.0015
			Spatial direction		
	h	1	1/2	1/4	1/8
	e_1^{h,τ_0}	2.2153E-02	4.9362E-04	2.8204E-08	8.0481E-13
	e_0^{h,τ_0}	2.1108E-02	4.6762E-04	2.5627E-08	7.9953E-13
	e_{-1}^{h,τ_0}	2.2153E-02	4.9362E-04	2.8204E-08	8.0492E-13

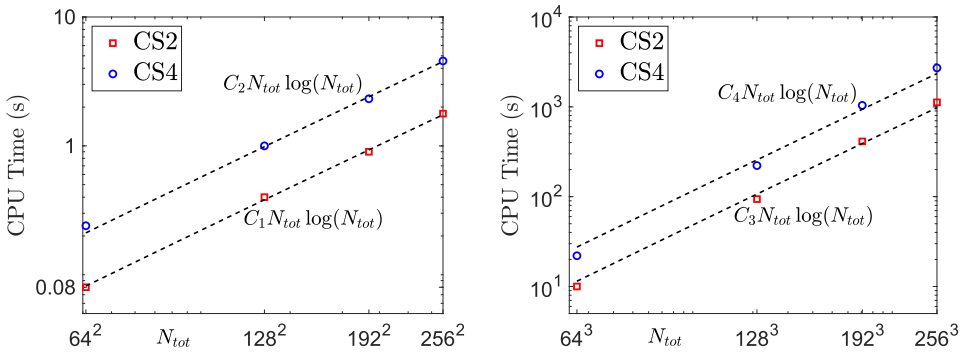

Fig. 1. Log–log plot of CPU time for CS2 and CS4 versus the total grid number N_{tot} for 2D (left) and 3D (right) cases in Example 3.

Table 4. Number of one-dimensional FFT/iFFT operators per time step for CS2/CS4 and ADI2/ADI4 methods in Example 4.

	Order	Method	Number of FFT/iFFT pairs
2D	Second	CS2	$12N$
		ADI2	$12N$
	Fourth	CS4	$24N$
		ADI4	$84N$
3D	Second	CS2	$18N^2$
		ADI2	$24N^2$
	Fourth	CS4	$36N^2$
		ADI4	$168N^2$

scheme[38] and refer to it as *ADI4*. We compare CS2/CS4 with ADI2/ADI4 methods in terms of efficiency, measured by the number of FFT/iFFT operations.

Table 4 presents the efficiency (measured by the number of FFT/iFFT operations) of the CS2/CS4 and ADI2/ADI4 methods. From these results, we can see that our method performs better in efficiency, and the superiority becomes more prominent as the convergence order increases. Consequently, we conclude that the compact splitting method facilitates the design of high-order schemes.

3.3. *Property verification*

In this subsection, we study the dynamical properties, including the energy/mass/magnetization conservation, evolution of angular momentum expectation and condensate widths, and carry out a comparison on the rotational symmetry conservation with the ADI method.

Example 5. (Dynamics of the mass and magnetization) Define the *mass* (or density) of the spin component $m_F = \ell$ as

$$N_\ell(t) := \int_{\mathbb{R}^d} |\psi_\ell(\mathbf{x}, t)|^2 \mathrm{d}\mathbf{x}, \quad t \geq 0, \ \ \ell = -1, 0, 1.$$

We choose $d = 2$, $\Omega = 0.6$, $\beta_n = 100$ and the initial data (3.1). Figure 2 shows time evolution of the mass of each component $N_j(t)$, the total mass $N(t)$, the magnetization $M(t)$ and the energy $E(t)$ for the following five sets of parameters:

- **Case 1**: $\beta_s = 0$, $B = 0$, $E_1 = 1$, $E_0 = 2$, $E_{-1} = 4$.
- **Case 2**: $\beta_s = 50$, $B = 0$, $E_1 = 1$, $E_0 = 2$, $E_{-1} = 4$.
- **Case 3**: $\beta_s = 0$, $B = 2$, $E_1 = E_0 = E_{-1} = 1$.
- **Case 4**: $\beta_s = 50$, $B = 2$, $E_1 = 1$, $E_0 = 2$, $E_{-1} = 3$.
- **Case 5**: $\beta_s = 50$, $B = 2$, $E_1 = 1$, $E_0 = 2$, $E_{-1} = 4$.

From Fig. 2, we can draw the following conclusions: (i) the total mass $N(t)$ is always conserved. (ii) When $\beta_s = 0$, if furthermore $B = 0$, then the mass of each

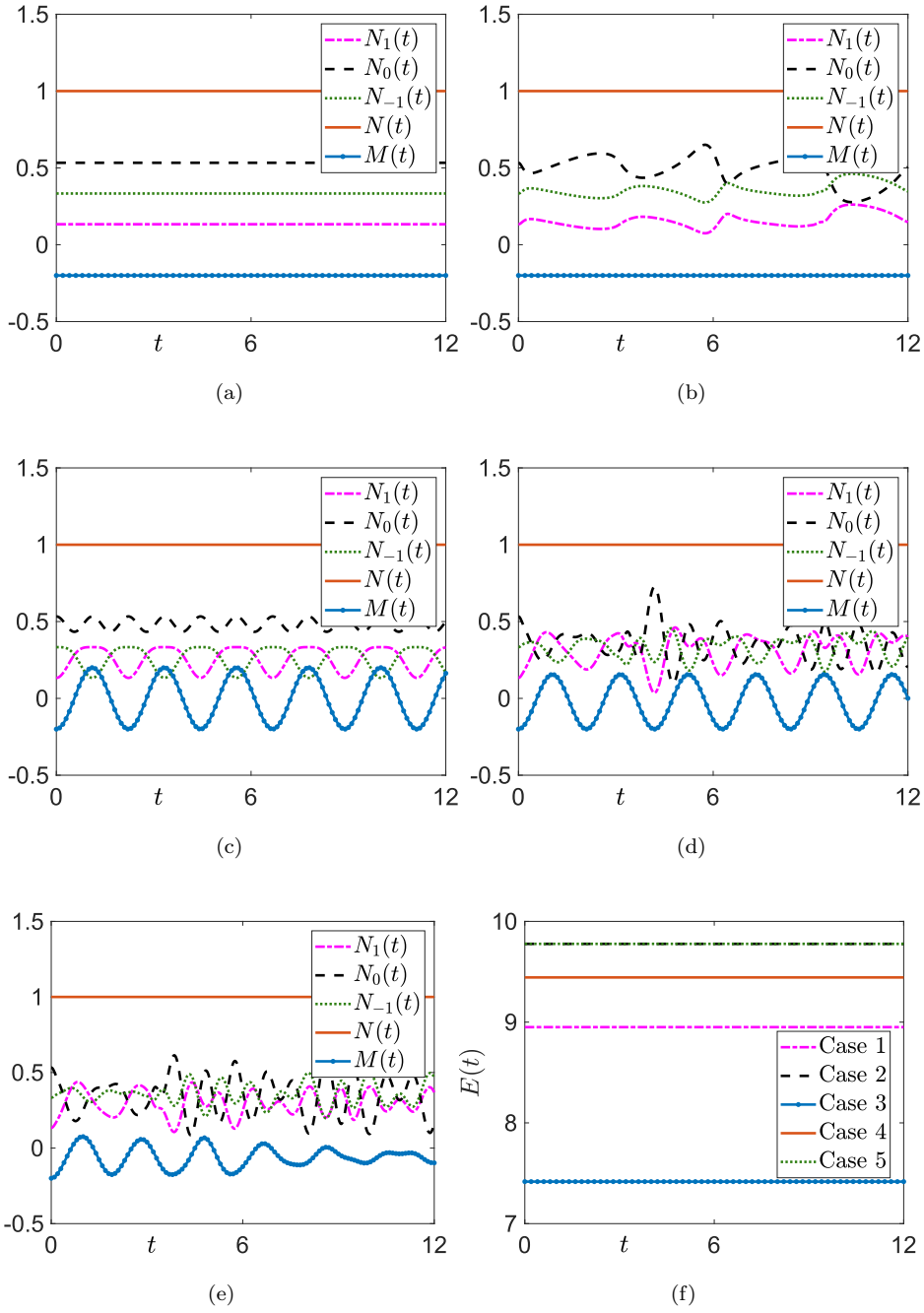

Fig. 2. Evolution of $N_j(t)$, $N(t)$, $M(t)$ for (a) Case 1, (b) Case 2, (c) Case 3, (d) Case 4, (e) Case 5 and $E(t)$ for (f) Cases 1–5 in Example 5.

component is also conserved (cf. Fig. 2(a)), otherwise, it evolves periodically if $B \neq 0$ (cf. Fig. 2(c)). (iii) When $B = 0$, the magnetization is conserved (cf. Figa. 2(a) and 2(b)). (iv) When $B \neq 0$ but $E_1 + E_{-1} = 2E_0$, the magnetization evolves periodically (cf. Figs. 2(c) and 2(d)). These are consistent with the dynamical laws derived in Ref. 11.

Example 6. (Dynamics of the angular momentum expectation) As a measure of vortex flux, we define the total *angular momentum expectation*

$$\langle L_z\rangle(t) = \sum_{\ell=-1}^{1} \langle L_z\rangle_\ell(t) \quad \text{with } \langle L_z\rangle_\ell(t) = \int_{\mathbb{R}^d} \bar{\psi}_\ell(\mathbf{x},t) L_z \psi_\ell(\mathbf{x},t)\mathrm{d}\mathbf{x}, \quad t \geq 0.$$

In fact, $\langle \widetilde{L}_z\rangle_\ell(t) := \langle L_z\rangle_\ell(t) \,/\, N_\ell(t)$ is the angular momentum expectation of the ℓ-th component. In our simulations, we choose $\Omega = 0.6$, $\beta_n = 100$, $E_1 = 1$, $E_0 = 0$, $E_{-1} = 2$, and the initial data

$$\psi_\ell^0(\mathbf{x}) = Ce^{-\frac{r^2}{2}} r^{m_\ell} e^{im_\ell\theta},$$

where the constant C is chosen such that the initial data satisfies the normalization (1.8). Figure 3 shows evolution of the angular momentum expectation for the following four sets of parameters

- **Case 1**: $\gamma_x = \gamma_y = 1$, $\beta_s = B = 0$, $m_1 = 1$, $m_0 = 0$, $m_{-1} = 2$.
- **Case 2**: $\gamma_x = \gamma_y = 1$, $\beta_s = 50$, $B = 2$, $m_1 = 1$, $m_0 = 0$, $m_{-1} = 2$.
- **Case 3**: $\gamma_x = \gamma_y = 1$, $\beta_s = 50$, $B = 2$, $m_1 = m_0 = m_{-1} = 1$.
- **Case 4**: $\gamma_x = 1$, $\gamma_y = 2$, $\beta_s = 50$, $B = 2$, $m_1 = m_0 = m_{-1} = 1$.

From Fig. 3, we can draw the following conclusions: (i) if $\gamma_x = \gamma_y$, $\langle L_z\rangle(t)$ is conserved for any time $t \geq 0$ (cf. Figs. 3(a)–3(c)). Furthermore, if $\beta_s = B = 0$ or $m_1 = m_0 = m_{-1} := m$, $\langle \widetilde{L}_z\rangle_\ell(t)$ is also conserved (cf. Figs. 3(a) and 3(c)). In addition, if $\beta_s = B = 0$, $\langle L_z\rangle_\ell(t)$ is also conserved (cf. Fig. 3(a)). (ii) If $\gamma_x \neq \gamma_y$, $\langle L_z\rangle(t)$ and relate quantities $\langle L_z\rangle_\ell(t)$, $\langle \widetilde{L}_z\rangle_\ell(t)$ are, in general, not conserved (cf. Fig. 3(d)). These observations agree well with the analytical results in Ref. 11.

Example 7. (Dynamics of condensate widths) Another important quantity characterizing the dynamics of the spin-1 BEC is the *condensate width* in the ν-direction (where $\nu = x, y, z$) defined as $\sigma_\nu = \sqrt{\delta_\nu(t)}$, where

$$\delta_\nu(t) = \sum_{\ell=-1}^{1} \delta_{\nu,\ell}(t) \quad \text{with } \delta_{\nu,\ell}(t) = \int_{\mathbb{R}^d} \nu^2 \left|\psi_\ell(\mathbf{x},t)\right|^2 \mathrm{d}\mathbf{x}.$$

We choose $\Omega = 0.6$, $\beta_n = 100$, $\beta_s = 50$, $B = 0$, $E_\ell = 0$, and the initial data

$$\psi_1^0(\mathbf{x}) = \phi(\mathbf{x}), \quad \psi_0^0(\mathbf{x}) = 3\sqrt{2}\phi(\mathbf{x}), \quad \psi_{-1}^0(\mathbf{x}) = \phi(\mathbf{x}), \tag{3.2}$$

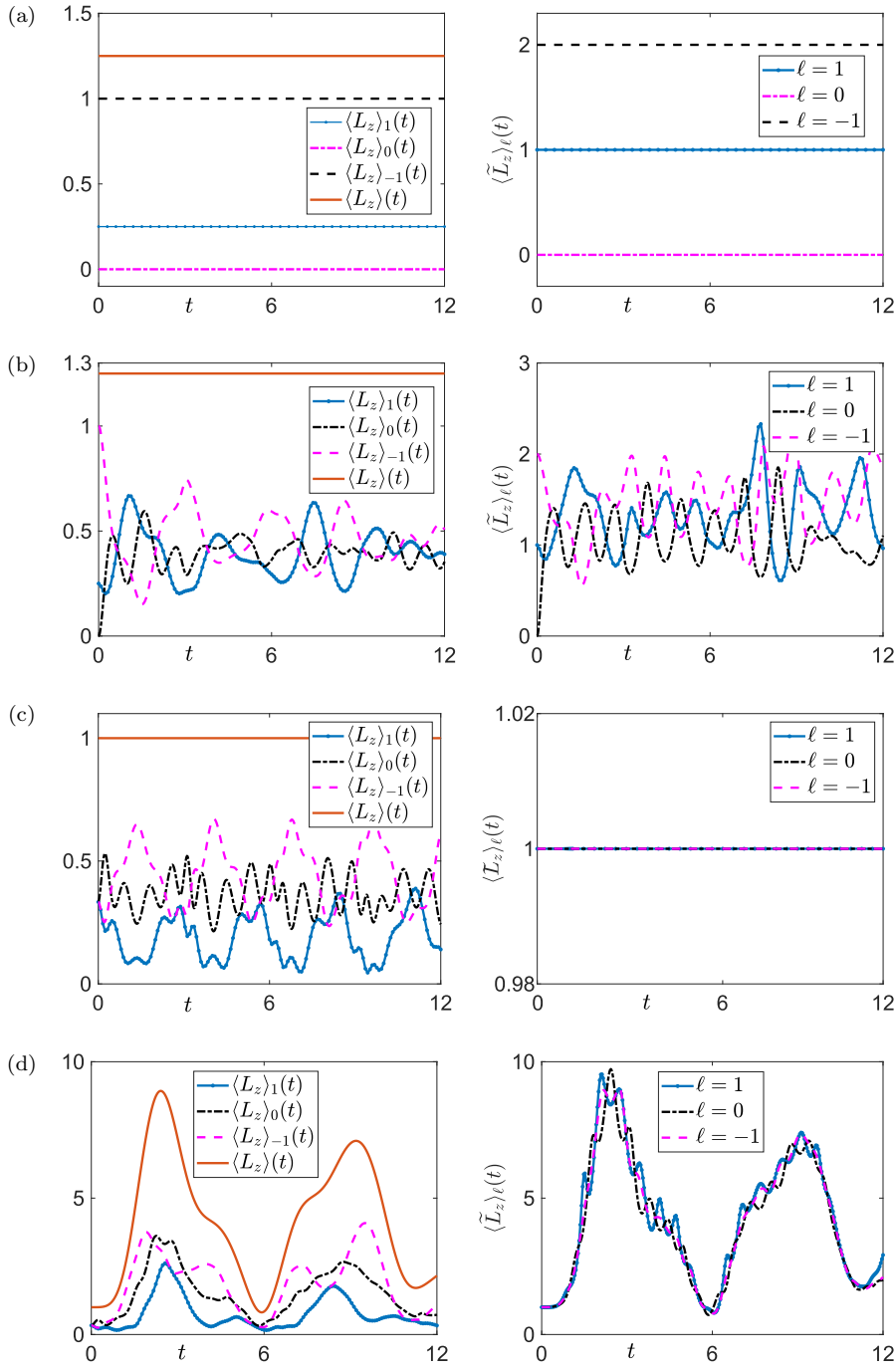

Fig. 3. Evolution of angular momentum expectation in Example 6 for Cases 1–4 (from top to bottom).

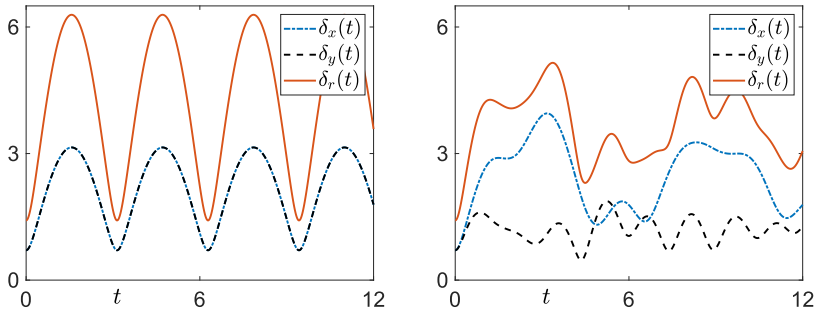

Fig. 4. Evolution of the condensate widths in Example 7 for (a) Case 1 and (b) Case 2.

with $\phi(\mathbf{x}) = \sqrt{0.05/\pi}e^{-|\mathbf{x}|^2/2}$. Figure 4 shows evolution of the condensate widths $\delta_x(t)$, $\delta_y(t)$ and $\delta_r(t) := \delta_x(t) + \delta_y(t)$ for the following two sets of parameters

- **Case 1**: $\gamma_x = 1$, $\gamma_y = 1$.
- **Case 2**: $\gamma_x = 1$, $\gamma_y = 2$.

From Fig. 4, we can see that the condensate width $\delta_r(t)$ is a periodic function when $\gamma_x = \gamma_y$, $B = 0$ and $E_\ell = 0$. While they are not periodic when $\gamma_x \neq \gamma_y$. These are consistent with the dynamical laws derived in Ref. 11.

Example 8. (Rotational symmetry) We investigate the rotational symmetry preservation property of two numerical methods, i.e. ADI scheme[36] and CS2. That is, for solution starting with initial value $\psi_\ell^0(\mathbf{x}_{jk})$ and $\widetilde{\psi}_\ell^0(\mathbf{x}_{jk}) = \psi_\ell^0(R(\theta)\mathbf{x}_{jk})$, $\widetilde{\psi}_\ell(\mathbf{x}_{jk}, t)$ is also the θ-rotation of $\psi_\ell(\mathbf{x}_{jk}, t)$ at time t, i.e. $\widetilde{\psi}_\ell(\mathbf{x}_{jk}, t) = \psi_\ell(R(\theta)\mathbf{x}_{jk}, t)$. Here, we define the following error function:

$$\mathcal{E}_\ell^{sym}(t) := \max_{\mathbf{x}_{jk}\in\mathcal{G}} |\psi_\ell(R(\theta)\mathbf{x}_{jk}, t) - \widetilde{\psi}_\ell(\mathbf{x}_{jk}, t)| / \max_{\mathbf{x}_{jk}\in\mathcal{G}} |\psi_\ell(R(\theta)\mathbf{x}_{jk}, t)|.$$

In our simulation, we choose $\Omega = 0.4$ and consider the following two cases:

- **Case 1**: $\beta_n = 1$, $\beta_s = 1$, $B = 1$, $E_1 = 3$, $E_0 = 2$, $E_{-1} = 1$.
- **Case 2**: $\beta_n = 10$, $\beta_s = 5$, $B = 0$, $E_1 = E_0 = E_{-1} = 0$.

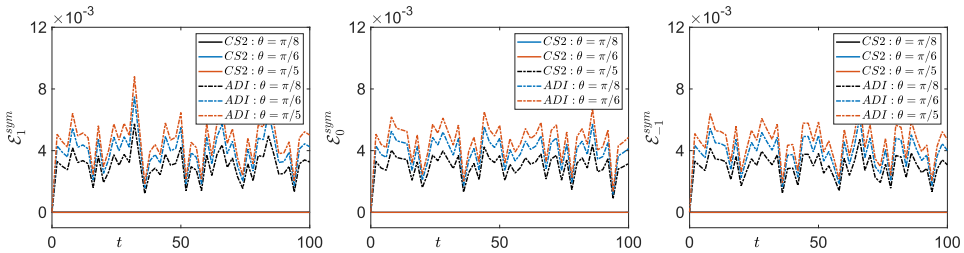

Fig. 5. Errors of the rotational symmetry preservation for Case 1 in Example 8.

The initial data is chosen as

$$\psi_1^0(\mathbf{x}) = \phi(\mathbf{x}), \quad \psi_0^0(\mathbf{x}) = 4\sqrt{3}\phi(\mathbf{x}), \quad \psi_{-1}^0(\mathbf{x}) = \phi(\mathbf{x}),$$

where $\phi(x,y) = \sqrt{0.02/\pi}e^{-(x^2+y^2)/2}(x+iy)$ for Case 1 and $\phi(x,y) = \sqrt{0.02/\pi}e^{-(x^2+y^2)/2}$ for Case 2.

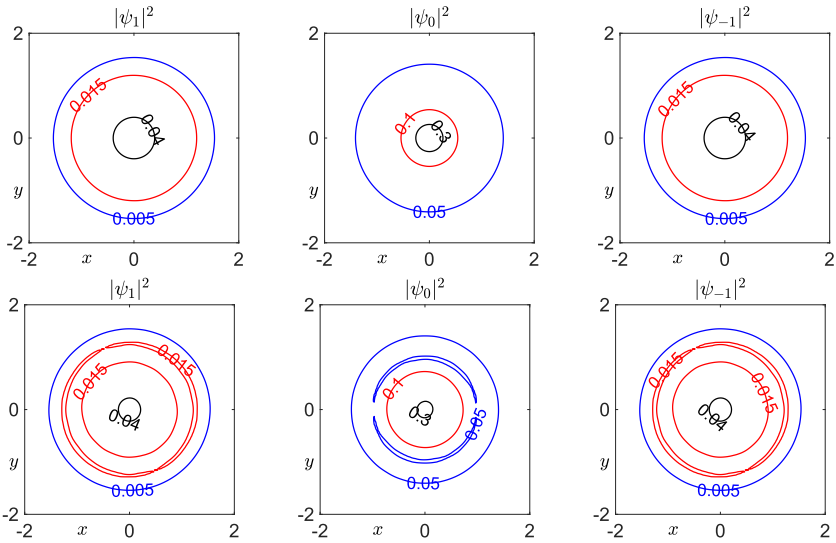

Fig. 6. Densities computed by CS2 (top) and ADI (bottom) for Case 2 in Example 8.

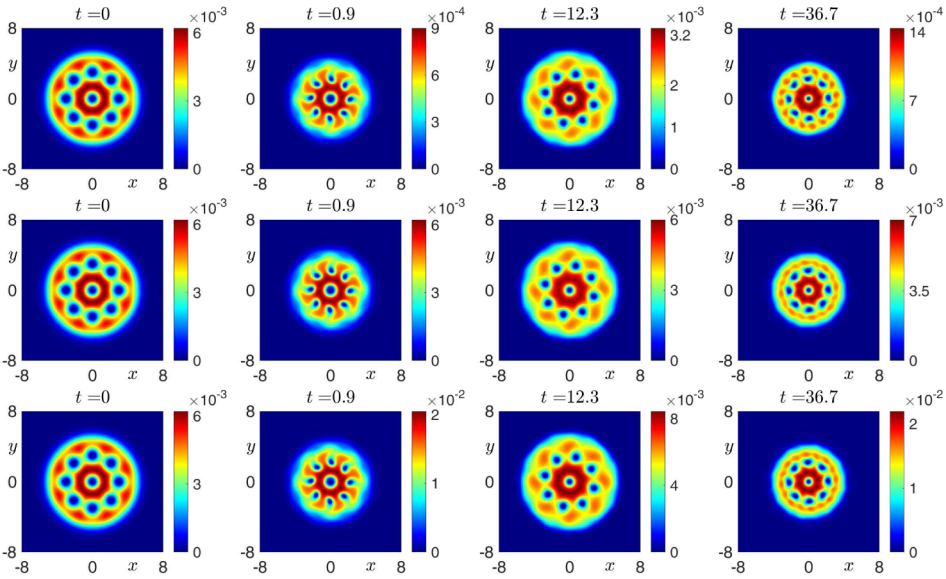

Fig. 7. Contour plots of the densities $|\psi_\ell|^2$ ($\ell = 1, 0, -1$, from top to bottom) in Example 9.

In practice, we choose $\mathbf{R}_L = [-32, 32]^2$, $h = 1/16$ and $\tau = 0.2$ for Case 1, while we choose $h = 1/32$ and $\tau = 0.2$ for Case 2. Figure 5 presents the errors $\mathcal{E}_\ell^{sym}(t)$ over the interval $t \in [0, 100]$ for CS2 and ADI in Case 1, while Fig. 6 shows the contour plots of the densities at time $t = 22$ in Case 2. From Figs. 5 and 6,

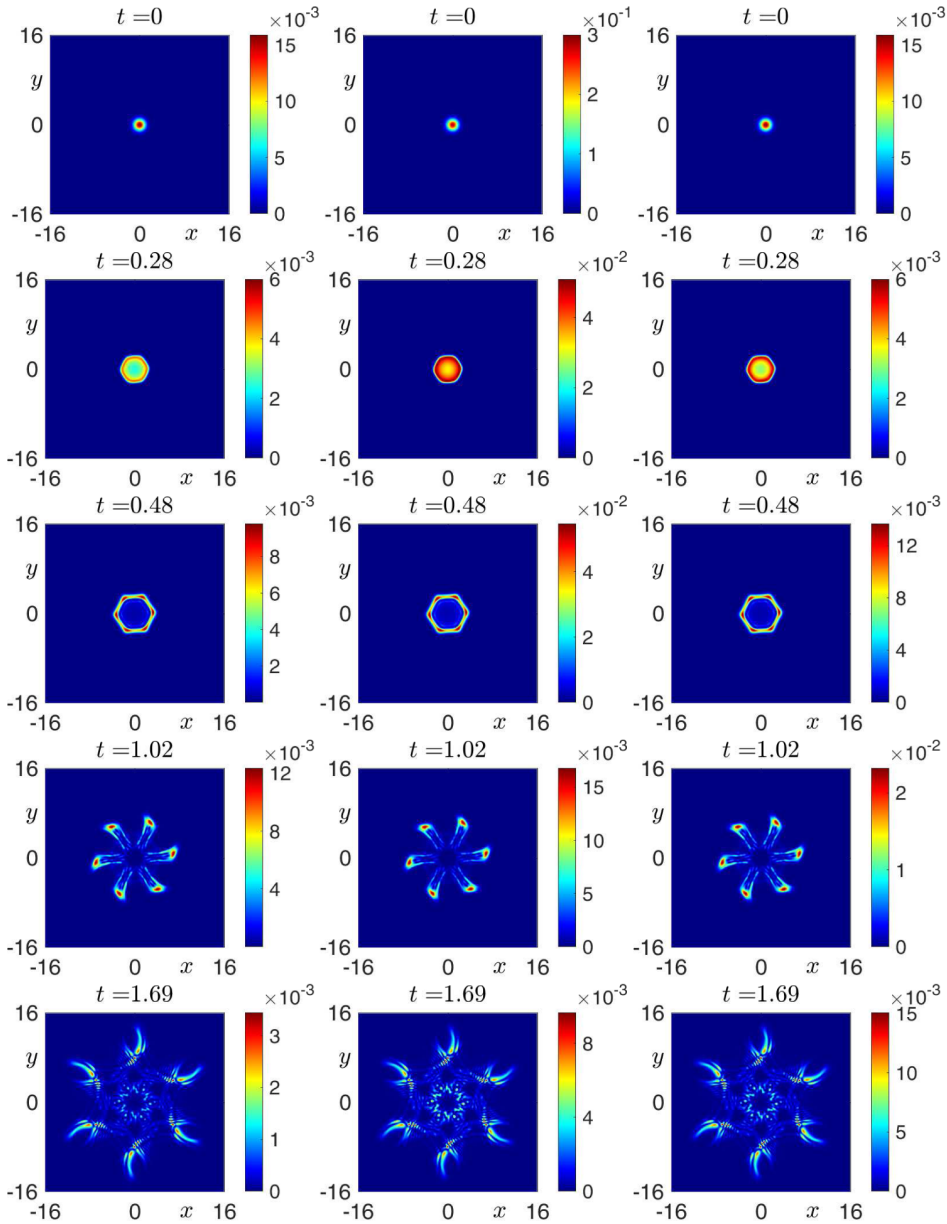

Fig. 8. Contour plots of the densities $|\psi_\ell|^2$ ($\ell = 1, 0, -1$, from left to right) in Example 10.

we conclude that ADI scheme does not keep rotational symmetry, while the CS2 method does. We refer the readers to Lemma 2.5 for a rigorous proof.

3.4. *Applications*

In the following, we study the evolution of quantized vortices and dynamics under honeycomb potential in rotating spin-1 BECs.

Example 9. (Dynamics of quantized vortices) Here, we choose $\beta_n = 200$, $\beta_s = 5$, $E_1 = 1$, $E_0 = E_{-1} = 2$, $B = 1$, $\Omega = 0.6$. The initial data is chosen as[7, 31]

$$\psi_\ell(x,y) = Ce^{-\frac{x^2+y^2}{4}} \prod_{j=1}^{9}[(x-x_j)+i(y-y_j)], \quad \ell = 1,0,-1,$$

where $(x_j, y_j) \in \{(0,0),(\pm 3,0),(0,\pm 3),(\pm 3\sqrt{2}/2, \pm 3\sqrt{2}/2)\}$ and the constant C is chosen such that the initial data satisfies the normalization (1.8).

In our simulation, we adopt CS4 scheme with $\tau = 10^{-3}$ and $h = 1/8$. Figure 7 shows the contour plots of the densities $|\psi_\ell|^2(\ell = 1,0,-1)$ at different time.

Example 10. (Dynamics under honeycomb potential) In the following, we study the dynamics under honeycomb potential

$$V(\mathbf{x}) = 10\,[\cos(\boldsymbol{b_1}\cdot\mathbf{x}) + \cos(\boldsymbol{b_2}\cdot\mathbf{x}) + \cos((\boldsymbol{b_1}+\boldsymbol{b_2})\cdot\mathbf{x})]$$

in rotating spin-1 BECs, where $\boldsymbol{b_1} = \frac{\pi}{4}(\sqrt{3},1)^\top$ and $\boldsymbol{b_2} = \frac{\pi}{4}(-\sqrt{3},1)^\top$. We choose the parameters $\Omega = 0.4, \beta_n = 5, \beta_s = -5, B = 1, E_1 = 1, E_0 = 2, E_{-1} = 1$ and the initial data (3.2).

In our simulation, we adopt CS4 scheme with $\tau = 10^{-3}$ and $h = 1/16$. Figure 8 shows the contour plots of the densities $|\psi_\ell|^2$ $(\ell = 1,0,-1)$ at different time.

4. Conclusions

We developed high-order compact splitting Fourier spectral methods to simulate the dynamics of rotating spin-1 BEC held in the external Ioffe-Pritchard magnetic field. We split the Hamiltonian into the linear part (Laplace, rotation and Zeeman energy) and the nonlinear part (all the others terms). The linear operator is decomposed into a product of five sub-operators with analytical splitting coefficients, and all these sub-operators are integrated exactly in either physical space or phase space. For the nonlinear subproblem, we derive an exact time-dependent formula for the spin vector, therefore, this nonlinear subproblem is reduced to a linear one. Then we design explicit high-order schemes using Magnus integrators. Based on such compact splitting, we can easily construct high-order spectral methods to simulate the dynamics.

Our approach is explicit, achieves high-order temporal convergence and spatial spectral accuracy, and conserves the mass and magnetization (when $B = 0$)

on discrete level. Additionally, it is unconditionally stable, time reversible, time transverse invariant and rotational symmetry preservation. Ample numerical results demonstrate the effectiveness in simulating the dynamics of rotating spin-1 BEC. Furthermore, the EEI method is simple to implement and can be easily adapted to rotating systems, such as the rotating spin-F BECs or BECs under the arbitrary-angle rotation with/without dipole-dipole interactions.[27, 33]

Appendix A. Fourth-Order Magnus Integrator

Here, we provide a detailed derivation for the fourth-order integrator ((2.14) and (2.16)). Specifically,

$$\Psi^{n+1}(\mathbf{x}) = e^{-i\tau(V+\beta_n\rho^n)}e^{-i\mathbf{S}_{4\text{th}}}\Psi^n(\mathbf{x}),$$

where

$$\mathbf{S}_{4\text{th}} = \int_0^\tau \mathbf{S}(t_n+\sigma)\mathrm{d}\sigma + \frac{1}{2}i\int_0^\tau \left[\int_0^\sigma \mathbf{S}(t_n+\mu)\mathrm{d}\mu, \mathbf{S}(t_n+\sigma)\right]\mathrm{d}\sigma,$$

with $\mathbf{S} = \beta_s\mathbf{F}\cdot\mathbf{f} + \mathbf{B}$. In fact, $\mathbf{S}_{4\text{th}}$ is a Hermitian matrix with the same structure as the $\mathbf{S}_{2\text{nd}}$ (2.18) with matrix entries

$$\alpha = \int_0^\tau \tilde{\alpha}_n(\sigma)\mathrm{d}\sigma + \frac{1}{2}i\int_0^\tau \left[\tilde{\alpha}_n(\sigma)\int_0^\sigma \tilde{\beta}_n(\mu)\mathrm{d}\mu - \tilde{\beta}_n(\sigma)\int_0^\sigma \tilde{\alpha}_n(\mu)\mathrm{d}\mu\right]\mathrm{d}\sigma,$$

$$\beta = \int_0^\tau \tilde{\beta}_n(\sigma)\mathrm{d}\sigma + \frac{1}{2}i\int_0^\tau \left[\overline{\tilde{\alpha}}_n(\sigma)\int_0^\sigma \tilde{\alpha}_n(\mu)\mathrm{d}\mu - \tilde{\alpha}_n(\sigma)\int_0^\sigma \overline{\tilde{\alpha}}_n(\mu)\mathrm{d}\mu\right]\mathrm{d}\sigma,$$

with $\tilde{\alpha}_n(\sigma) = \tilde{\alpha}(t_n+\sigma)$, $\tilde{\alpha}(t) := \beta_s F_-(t)/\sqrt{2}+B$ and $\tilde{\beta}(t) := \beta_s F_z(t)$. Both integrals can be computed analytically, i.e.

$$\begin{aligned}\alpha = {} & -\frac{i\beta_s}{2B}[\sin(\sqrt{2}B\tau)F_y^n + (\cos(\sqrt{2}B\tau)-1)F_z^n] + \left(\frac{\beta_s}{\sqrt{2}}F_x^n + B\right)\tau \\ & + \frac{\beta_s}{2\sqrt{2}B}\left[i\left(\frac{\beta_s}{\sqrt{2}}F_x^n + B\right)((F_z^n s_1 - F_y^n c_1) - \sqrt{2}B(F_y^n s_2 + F_z^n c_2)) \right. \\ & \left. + \frac{\beta_s c_1}{\sqrt{2}}((F_y^n)^2 + (F_z^n)^2)\right], \end{aligned} \tag{A.1}$$

$$\begin{aligned}\beta = {} & \frac{\beta_s}{\sqrt{2}B}[\sin(\sqrt{2}B\tau)F_z^n - (\cos(\sqrt{2}B\tau)-1)F_y^n] \\ & + \frac{\beta_s}{2B}\left(\frac{\beta_s}{\sqrt{2}}F_x^n + B\right)[(F_y^n s_1 + F_z^n c_1) + \sqrt{2}B(F_z^n s_2 - F_y^n c_2)], \end{aligned} \tag{A.2}$$

where $s_1 = \frac{1}{\sqrt{2}B}[1-\cos(\sqrt{2}B\tau)]$, $s_2 = \frac{1}{2B^2}[-\sqrt{2}B\tau\cos(\sqrt{2}B\tau) + \sin(\sqrt{2}B\tau)]$, $c_1 = \frac{1}{\sqrt{2}B}\sin(\sqrt{2}B\tau) - \tau$ and $c_2 = \frac{1}{2B^2}[-1+\cos(\sqrt{2}B\tau) + \sqrt{2}B\tau\sin(\sqrt{2}B\tau)]$.

We can obtain the explicit expression for $\mathbf{G}_{4\text{th}} := e^{-i\mathbf{S}_{4\text{th}}}$ in a similar way as $\mathbf{G}_{2\text{nd}} = e^{-i\mathbf{S}_{2\text{nd}}}$ (2.21). Therefore, the matrix $\mathbf{G}_{4\text{th}}$ remains in the form of $\mathbf{G}_{2\text{nd}}$ (2.21), and the only modification is to replace α and β in $\mathbf{G}_{2\text{nd}}$ with the expressions given in (A.1)–(A.2). Then the fourth-order integrator reads as (2.23).

Appendix B. Exact Solution for Laplace-Rotation Problem

Here, we derive the exact solution to the following Laplace-Rotation subproblem

$$\begin{cases} i\partial_t \psi(\mathbf{x},t) = \left[-\frac{1}{2}\Delta - \Omega L_z\right]\psi(\mathbf{x},t), \\ \psi(\mathbf{x},0) = \psi_0(\mathbf{x}). \end{cases} \tag{B.1}$$

We define a new function by rotation mapping,[9] specifically,

$$\phi(\mathbf{x},t) := \psi(\mathcal{R}(t)\mathbf{x},t), \quad \mathbf{x}\in\mathbb{R}^d, \quad t\geq 0,$$

where the orthogonal rotational matrix

$$\mathcal{R}(t) = \begin{pmatrix} \cos(\Omega t) & \sin(\Omega t) \\ -\sin(\Omega t) & \cos(\Omega t) \end{pmatrix}, \quad \text{if } d=2,$$

$$\mathcal{R}(t) = \begin{pmatrix} \cos(\Omega t) & \sin(\Omega t) & 0 \\ -\sin(\Omega t) & \cos(\Omega t) & 0 \\ 0 & 0 & 1 \end{pmatrix}, \quad \text{if } d=3.$$

Using the chain rule, it becomes evident that ϕ satisfies the following equations:

$$\begin{cases} i\partial_t \phi(\mathbf{x},t) = -\frac{1}{2}\Delta\phi(\mathbf{x},t), \\ \phi(\mathbf{x},0) = \psi(\mathbf{x},0) = \psi_0(\mathbf{x}). \end{cases} \tag{B.2}$$

We can explicitly solve the above equation in Fourier space,[25] to be exact,

$$\hat{\phi}_{\mathbf{k}}(t) = e^{-\frac{1}{2}it|\mathbf{k}|^2}\hat{\psi}_{\mathbf{k}}(0) \quad \text{with } \hat{\psi}_{\mathbf{k}}(0) = \int_{\mathbb{R}^d} \psi(\mathbf{x},0)e^{-i\mathbf{k}\cdot\mathbf{x}}\mathrm{d}\mathbf{x}.$$

This leads to the solution in physical space after an inverse Fourier transform

$$\phi(\mathbf{x},t) = \frac{1}{(2\pi)^d}\int_{\mathbb{R}^d} e^{-\frac{1}{2}it|\mathbf{k}|^2}\hat{\psi}_{\mathbf{k}}(0)e^{i\mathbf{k}\cdot\mathbf{x}}\mathrm{d}\mathbf{k}.$$

Then, we can obtain the exact solution of equation (B.1) by

$$\psi(\mathbf{x},t) = \phi(\mathcal{R}^{-1}(t)\mathbf{x},t). \tag{B.3}$$

Specifically, we provide the explicit expression of exact solution using the initial value

$$\psi(\mathbf{x},0) = \frac{1}{\pi^{1/4}}x^2 e^{-\frac{x^2+y^2}{2}}.$$

A simple calculation shows that

$$\begin{aligned} \hat{\psi}_{\mathbf{k}}(0) &= \frac{1}{\pi^{1/4}}\left[\int_{\mathbb{R}} e^{-\frac{1}{2}y^2}e^{-ik_2 y}\mathrm{d}y\right]\left[\int_{\mathbb{R}} x^2 e^{-\frac{1}{2}x^2}e^{-ik_1 x}\mathrm{d}x\right] \\ &= \frac{2\pi}{\pi^{1/4}}e^{-\frac{1}{2}k_2^2}[-\partial_{k_1 k_1}e^{-\frac{1}{2}k_1^2}] \\ &= \frac{2\pi}{\pi^{1/4}}(1-k_1^2)e^{-\frac{1}{2}(k_1^2+k_2^2)}. \end{aligned}$$

Let $\tilde{x} = \frac{x}{\sqrt{1+it}}, \tilde{y} = \frac{y}{\sqrt{1+it}}$, we have

$$\begin{aligned}
\phi(x,y,t) &= \frac{1}{\pi^{1/4}}\frac{1}{2\pi}\left[\int_{\mathbb{R}} e^{-\frac{1}{2}itk_2^2}e^{-\frac{1}{2}k_2^2}e^{ik_2y}\mathrm{d}k_2\right]\left[\int_{\mathbb{R}}(1-k_1^2)e^{-\frac{1}{2}itk_1^2}e^{-\frac{1}{2}k_1^2}e^{ik_1x}\mathrm{d}k_1\right] \\
&= \frac{1}{\pi^{1/4}}\frac{1}{2\pi}\frac{1}{(1+it)}\left[\int_{\mathbb{R}} e^{-\frac{1}{2}k_2^2}e^{ik_2\tilde{y}}\mathrm{d}k_2\right]\left(1+\frac{1}{it+1}\partial_{\tilde{x}\tilde{x}}\right)\left[\int_{\mathbb{R}} e^{-\frac{1}{2}k_1^2}e^{ik_1\tilde{x}}\mathrm{d}k_1\right] \\
&= \frac{1}{\pi^{1/4}}\frac{1}{(1+it)}\left[1-\frac{1}{1+it}(1-\tilde{x}^2)\right]e^{-\frac{1}{2}(\tilde{x}^2+\tilde{y}^2)} \\
&= \frac{1}{\pi^{1/4}}\frac{x^2-t^2+it}{(1+it)^3}e^{-\frac{1}{2(it+1)}(x^2+y^2)}.
\end{aligned}$$

Using (B.3), we have

$$\begin{aligned}
\psi(x,y,t) = \phi(\mathcal{R}^{-1}(t)\mathbf{x},t) &= \frac{1}{\pi^{1/4}}\frac{x_1^2-t^2+it}{(1+it)^3}e^{-\frac{1}{2(it+1)}(x_1^2+y_1^2)} \\
&= \frac{1}{\pi^{1/4}}\frac{x_1^2-t^2+it}{(1+it)^3}e^{-\frac{1}{2(it+1)}(x^2+y^2)},
\end{aligned}$$

where $x_1 = \cos(\Omega t)x - \sin(\Omega t)y$ and $y_1 = \sin(\Omega t)x + \cos(\Omega t)y$.

Acknowledgment

This work was partially supported by the National Key R&D Program of China No. 2024YFA1012803 (Y. Zhang and Q. Tang), the National Natural Science Foundation of China No. 12271400 (X. Liu, X. Meng and Y. Zhang), No. 11971335 (Q. Tang), and the Natural Science Foundation of Sichuan Province No. 2024NSFSC0438 (Q. Tang).

ORCID

Xin Liu https://orcid.org/0009-0001-6268-5100

Xiangyu Meng https://orcid.org/0009-0000-1712-7380

Qinglin Tang https://orcid.org/0009-0006-7574-8023

Yong Zhang https://orcid.org/0000-0002-5759-6744

References

1. P. Alphonse and J. Bernier, Polar decomposition of semigroups generated by non-selfadjoint quadratic differential operators and regularizing effects, *Ann. Sci. de l'Ecole Norm. Superieure* **56** (2023) 323–382.
2. M. H. Anderson, J. R. Ensher, M. R. Matthewa, C. E. Wieman and E. A. Cornell, Observation of Bose–Einstein condensation in a dilute atomic vapor, *Science* **269** (1995) 198–201.
3. X. Antoine, W. Bao and C. Besse, Computational methods for the dynamics of the nonlinear Schrödinger/Gross–Pitaevskii equations, *Comput. Phys. Commun.* **184** (2013) 2621–2633.

4. W. Bao and Y. Cai, Mathematical models and numerical methods for spinor Bose–Einstein condensates, *Commun. Comput. Phys.* **24** (2018) 899–965.
5. W. Bao and Y. Cai, Mathematical theory and numerical methods for Bose-Einstein condensation, *Kinet. Relat. Models* **6** (2013) 1–135.
6. W. Bao, I. L. Chern and Y. Zhang, Efficient numerical methods for computing ground states of spin-1 Bose–Einstein condensates based on their characterizations, *J. Comput. Phys.* **253** (2013) 189–208.
7. W. Bao, H. Li and J. Shen, A generalized-Laguerre–Fourier–Hermite pseudospectral method for computing the dynamics of rotating Bose–Einstein condensates, *SIAM J. Sci. Comput.* **31** (2009) 3685–3711.
8. W. Bao and F. Y. Lim, Numerical methods for computing the ground state of spin-1 Bose–Einstein condensates in a uniform magnetic field, *Phys. Rev. E* **78** (2008) 066704.
9. W. Bao, D. Marahrens, Q. Tang and Y. Zhang, A simple and efficient numerical method for computing the dynamics of rotating Bose–Einstein condensates via rotating Lagrangian coordinates, *SIAM J. Sci. Comput.* **35** (2013) A2671–A2695.
10. W. Bao and H. Wang, An efficient and spectrally accurate numerical method for computing dynamics of rotating Bose–Einstein condensates, *J. Comput. Phys.* **217** (2006) 612–626.
11. W. Bao and Y. Zhang, Dynamical laws of the coupled Gross–Pitaevskii equations for spin-1 Bose–Einstein condensates, *Methods Appl. Anal.* **17** (2010) 49–80.
12. J. Bernier, Exact splitting methods for semigroups generated by inhomogeneous quadratic differential operators, *Found. Comput. Math.* **21** (2021) 1401–1439.
13. J. Bernier, N. Crouseilles and Y. Li, Exact splitting methods for kinetic and Schrödinger equations, *J. Sci. Comput.* **86** (2021) 1–35.
14. C. Besse, G. Dujardin and I. Lacroix-Violet, High order exponential integrators for nonlinear Schrödinger equations with application to rotating Bose–Einstein condensates, *SIAM J. Numer. Anal.* **55** (2017) 1387–1411.
15. C. C. Bradley, C. A. Sackett, J. J. Tollett and R. G. Hulet, Evidence of Bose–Einstein condensation in an atomic gas with attractive interaction, *Phys. Rev. Lett.* **75** (1995) 1687–1690.
16. E. N. Bulgakov and A. F. Sadreev, Vortex phase diagram of F=1 spinor Bose–Einstein condensates, *Phys. Rev. Lett.* **90** (2003) 200401.
17. M.-S. Chang, C. D. Hamley, M. D. Barrett, J. A. Sauer, K. M. Fortier, W. Zhang, L. You and M. S. Chapman, Observation of spinor dynamics in optically trapped ^{87}Rb Bose–Einstein Condensates, *Phys. Rev. Lett.* **92** (2004) 140403.
18. C. V. Ciobanu, S. K. Yip and T. L. Ho, Phase diagrams of F=2 spinor Bose–Einstein condensates, *Phys. Rev. A* **61** (2000) 033607.
19. T. L. Ho, Spinor Bose condensates in optical traps, *Phys. Rev. Lett.* **81** (1998) 742–745.
20. T. L. Ho and V. B. Shenoy, Binary mixtures of Bose condensates of alkali atoms, *Phys. Rev. Lett.* **77** (1996) 3276–3279.
21. M. Hochbruck and C. Lubich, On magnus integrator for time-dependent Schrödinger equations, *SIAM J. Numer. Anal.* **41** (2003) 945–963.
22. M. Hochbruck and A. Ostermann, Exponential integrators, *Acta Numer.* **19** (2010) 209–286.
23. K. Kasamatsu, M. Tsubota and M. Ueda, Vortex phase diagram in rotating two-component Bose–Einstein condensates, *Phys. Rev. Lett.* **91** (2003) 150406.
24. Y. Kawaguchi and M. Ueda, Spinor Bose–Einstein condensates, *Phys. Rep.* **520** (2012) 253–381.

25. C. Klein, J. Prada-Malagon and N. Stoilov, On numerical approaches to nonlinear Schrödinger and Korteweg–de Vries equations for piecewise smooth and slowly decaying initial data, *Physica D* **454** (2023) 133885.
26. X. Liu, Y. Yuan and Y. Zhang, An efficient compact splitting Fourier spectral method for computing the dynamcis of rotating spin-orbit coupled spin-1 Bose–Einstein condensates, *J. Comput. Phys.* **529** (2025) 113892.
27. S. B. Prasad, B. C. Mulkerin and A. M. Martin, Arbitrary-angle rotation of the polarization of a dipolar Bose–Einstein condensate, *Phys. Rev. A* **103** (2021) 033322.
28. H. Pu, C. K. Law, S. Raghavan, J. H. Eberly and N. P. Bigelow, Spin-mixing dynamics of a spinor Bose–Einstein condensate, *Phys. Rev. A* **60** (1999) 1463–1470.
29. W. Rossmann, *Lie Groups*: *An Introduction Through Linear Groups* (Oxford Univ. Press, 2006).
30. H. Schmaljohann, M. Erhard, J. Kronjager, K. Sengstock and K. Bongs, Dynamics and thermodynamics in spinor quantum gases, *Appl. Phys. B-Lasers O* **79** (2004) 1001–1008.
31. V. Schweikhard, I. Coddington, P. Engels, S. Tung and E. A. Cornell, Vortex-lattice dynamics in rotating spinor Bose–Einstein condensates, *Phys. Rev. Lett.* **93** (2003) 210403.
32. J. Shen, T. Tang and L. Wang, *Spectral Methods*: *Algorithms, Analysis and Applications* (Springer, 2011).
33. Q. Shu, Q. Tang, S. Zhang and Y. Zhang, A preconditioned Riemannian conjugate gradient method for computing the ground states of arbitrary-angle rotating Bose–Einstein condensates, *J. Comput. Phys.* **512** (2024) 113130.
34. L. M. Symes and P. B. Blakie, Solving the spin-2 Gross–Pitaevskii equation using exact nonlinear dynamics and symplectic composition, *Phys. Rev. E* **95** (2017) 013311.
35. L. M. Symes, R. I. McLachlan and P. B. Blakie, Efficient and accurate methods for solving the time-dependent spin-1 Gross–Pitaevskii equation, *Phys. Rev. E* **93** (2016) 053309.
36. H. Wang, A time-splitting spectral method for computing dynamics of spinor F=1 Bose–Einstein condensates, *Int. J. Comput. Math.* **84** (2007) 925–944.
37. H. Wang, J. Wang, S. Zhang and Y. Zhang, A time splitting Chebyshev–Fourier spectral method for the time-dependent rotating nonlocal Schrödinger equation in polar coordinates, *J. Comput. Phys.* **498** (2024) 112680.
38. H. Yoshida, Construction of higher order symplectic integrators, *Phys. Lett. A* **150** (1990) 262–268.